

HI content of selected mid-infrared bright, starburst blue compact dwarf galaxies

Yogesh Chandola^{1,2,3*}, Di Li^{1,4,5†}, Chao-Wei Tsai^{1,6,7‡}, Guodong Li^{1,7}, Yingjie Peng^{8,9},
Pei Zuo^{1,9,10}, Travis McIntyre¹, Yin-Zhe Ma^{11,2§}, Daniel Stern¹², Roger Griffith¹²,
Thomas Jarrett¹³, Peter Eisenhardt¹², Chantal Balkowski¹⁴

¹CAS Key Laboratory of FAST, National Astronomical Observatories, Chinese Academy of Sciences, Beijing-100101, China

²Purple Mountain Observatory, Chinese Academy of Sciences (CAS), 10, Yuan Hua Road, Qixia District, Nanjing, 210023, China

³Inter-University Centre for Astronomy and Astrophysics (IUCAA), Post bag 4, Ganeshkhind, Pune, 411007, India

⁴Research Center for Intelligent Computing Platforms, Zhejiang Laboratory, Hangzhou 311100, China

⁵NAOC-UKZN Computational Astrophysics Centre (NUCAC), University of KwaZulu-Natal, Durban, 4000, South Africa

⁶Institute for Frontiers in Astronomy and Astrophysics, Beijing Normal University, Beijing 102206, China

⁷University of Chinese Academy of Sciences, Beijing 100049, People's Republic of China

⁸Department of Astronomy, School of Physics, Peking University, 5 Yiheyuan Road, Beijing 100871, People's Republic of China

⁹Kavli Institute for Astronomy and Astrophysics, Peking University, 5 Yiheyuan Road, Beijing 100871, People's Republic of China

¹⁰International Centre for Radio Astronomy Research (ICRAR), University of Western Australia, 35 Stirling Highway, Crawley, WA 6009, Australia

¹¹Department of Physics, Stellenbosch University, Matieland 7602, South Africa

¹²Jet Propulsion Laboratory, California Institute of Technology, 4800 Oak Grove Drive, M/S 169-327, Pasadena, CA 91109, USA

¹³Department of Astronomy, University of Cape Town, Private Bag X3, Rondebosch, 7701, South Africa

¹⁴Observatoire de Paris, 61 Av. de l'Observatoire, 75014 Paris, France

4 October 2023

ABSTRACT

We report measurements of HI content in 11 nearby, actively star-forming, blue compact dwarf galaxies (BCDs) from 21 cm observations with the Arecibo telescope. These BCDs, selected by their red ($W2[4.6\ \mu\text{m}] - W3[12\ \mu\text{m}] > 3.8\ \text{mag}$) and bright mid-infrared (MIR) emission ($W4[22\ \mu\text{m}] < 7.6\ \text{mag}$), have high specific star formation rates (median sSFR $\sim 10^{-7.8}\ \text{yr}^{-1}$), similar to high redshift galaxies. HI emission was detected in six sources. We analyze our new detections in the context of previous HI observations of 218 dwarf irregulars (dIs) and BCDs in the literature. The $M_{\text{HI}} - M_*$ relation resulting from our observations confirms the dominating fraction of HI gas among baryons in galaxies with lower stellar masses. This Arecibo BCD sample has significantly lower median HI depletion timescales ($\tau_{\text{HI}} \sim 0.3\ \text{Gyr}$) than other dIs/BCDs ($\sim 6.3\ \text{Gyr}$) in the literature. The majority of the sources (10/11) in the Arecibo sample are very red in $W1[3.4\ \mu\text{m}] - W2[4.6\ \mu\text{m}]$ colour ($> 0.8\ \text{mag}$) implying the presence of warm dust. We investigate the relation of τ_{HI} with stellar mass (M_*) and sSFR. We find that τ_{HI} is significantly anti-correlated with M_* for higher sSFR ($> 10^{-8.5}\ \text{yr}^{-1}$) and with sSFR for higher stellar mass ($> 10^{7.5}\ M_{\odot}$) dwarf galaxies. The high sSFR for the BCDs in the Arecibo observed sample is mainly due to their high atomic gas star formation efficiency (SFE) or low τ_{HI} . The low τ_{HI} or high SFE in these sources is possibly due to runaway star formation in compact and dense super star clusters.

Key words: galaxies: dwarf – galaxies: starburst – galaxies: star formation – radio lines: galaxies

1 INTRODUCTION

Blue Compact Dwarf Galaxies (BCDs) are galaxies characterized spectroscopically by intense emission lines and blue, fainter optical continuum ($M_B > -18$; Zwicky 1966;

* E-mail: yogesh.chandola@pmo.ac.cn

† E-mail: dili@nao.cas.cn

‡ E-mail: cwtsai@nao.cas.cn

§ E-mail: mayinzhe@sun.ac.za

Gil de Paz et al. 2003). Their metallicities are low, ($Z < 1/2 Z_{\odot}$; Hunter & Hoffman 1999), and they have dramatically different physical properties compared to normal dwarf galaxies (Zwicky 1966; Gil de Paz et al. 2003). The great majority of BCDs are metal-poor, although BCDs with extremely low metallicity ($< 1/10 Z_{\odot}$) are rare (Izotov et al. 2012). There have been recent efforts to increase the numbers of extremely low metallicity BCDs (Kniazev et al. 2003; Morales-Luis et al. 2011; Izotov et al. 2012; James et al. 2015; Hirschauer et al. 2016; Sánchez Almeida et al. 2016, 2017; Guseva et al. 2017; Izotov et al. 2018; Hsyu et al. 2018). Generally, all BCDs host recent star formation, their optical blue colour indicating a starburst no older than a few Myr (Kunth 1999). Some BCDs have stars forming in compact regions (< 50 pc) while others form stars in spatially extended regions (> 100 pc) (Hirashita & Hunt 2004). This dichotomy of star formation activity in BCDs can affect the temperature of surrounding dust, and thus their mid-infrared (MIR) photometry from the *Wide-Infrared Survey Explorer* (*WISE*; Wright et al. 2010). The stronger MIR emission in compact active star-forming BCDs is dominated by hot (200–1500 K) small dust grains (size < 100 Å) heated by the starburst (Dale et al. 2001; Wu et al. 2006). Because of hot dust emission at ~ 10 μm , these BCDs have redder colours across *WISE* 3.4–12 μm bands (W1–W3: 3.4, 4.6, 12 μm). This provides a way to select actively star-forming, low metallicity ($\lesssim 1/8 Z_{\odot}$) and high specific star formation rate (sSFR $\gtrsim 10^{-8}$ yr^{-1}) BCDs (Griffith et al. 2011; Hainline et al. 2016; Satyapal et al. 2018). Objects with sSFR higher than 10^{-8} yr^{-1} are rare locally ($z < 0.05$), although similar objects such as green pea galaxies and Lyman- α Emitters are commonly found at higher redshifts ($z > 0.1$) (Gawiser et al. 2007; Amorín et al. 2010; Hainline et al. 2016; Yang et al. 2017).

While molecular gas is directly related to star-formation activity, cold atomic HI gas has a vital role as a fuel reservoir (Kennicutt & Evans 2012). Studying atomic gas content and gas depletion timescales provides insights into the evolution processes of galaxies. The dependence of gas to stellar mass ratios and star-formation efficiencies/depletion timescales on stellar masses and specific star formation rates have been investigated in recent HI and molecular gas surveys for local massive galaxies ($z < 0.05$, $M_{\star} > 10^9 M_{\odot}$; Schiminovich et al. 2010; Saintonge et al. 2011; Huang & Kauffmann 2014; Jaskot et al. 2015; Saintonge et al. 2017; Catinella et al. 2018). At lower stellar masses ($< 10^9 M_{\odot}$), HI 21cm emission from dwarf galaxies, including some BCDs have been studied using single-dish and interferometric facilities (Thuan & Martin 1981; Thuan et al. 2004; Huchtmeier et al. 2005, 2007; Pustilnik & Martin 2007; Filho et al. 2013; Thuan et al. 2016; Pustilnik et al. 2001; Thuan et al. 2004; Chengalur et al. 2006; Ekta et al. 2006, 2008, 2009; Ekta & Chengalur 2010; Huang et al. 2012a,b; Lelli et al. 2014a; Adams & Oosterloo 2018). Most of these sources have sSFR lower than 10^{-8} yr^{-1} and redshifts below 0.02. In this paper, we present deep HI observations of 11 local ($z < 0.033$, median redshift ~ 0.026) MIR-bright BCDs with an ongoing major episode of star formation with most of these having sSFR $\gtrsim 10^{-8}$ yr^{-1} . In addition to these sources, we collect information on several dwarf irregulars(dIs)/BCDs studied in HI from literature to provide

a comprehensive study of the relation between HI gas content and galaxy properties such as stellar mass and star-formation rate.

In this paper, we describe the sample for study in Section 2. In Section 2.1.1, details of observations with the Arecibo Observatory and data reduction procedure are given. Results are reported in Section 3. The methods of estimating the stellar mass and star formation rate are included in Section 4. We discuss our results in Section 5 and summarize them in Section 6. Magnitudes are reported in the Vega system. In this paper, we assume a concordance cosmology with $H_0 = 70$ $\text{km s}^{-1} \text{Mpc}^{-1}$, $\Omega_{\text{m}} = 0.3$, and $\Omega_{\Lambda} = 0.7$.

2 SAMPLE, OBSERVATION AND DATA REDUCTION

2.1 Sample of BCDs observed with Arecibo Observatory

MIR colours can be used to select actively star-forming, high specific star formation rate starburst BCDs. We selected dwarf galaxies ($M_{\star} \lesssim 3 \times 10^9 M_{\odot}$) with red *WISE* colour (W2–W3 > 3.8 mag) and bright MIR emission (W4 < 7.6 mag equivalent to W4 > 7.5 mJy) from All-*WISE* catalog (Cutri et al. 2021). The red MIR colours indicate they are likely undergoing a major starburst episode (Griffith et al. 2011; Hainline et al. 2016; Satyapal et al. 2018). The W2–W3 colour cut was empirically chosen to include the star-forming dwarfs discovered by the *WISE* in the early stage of the mission (Donoso et al. 2012; Tsai et al. 2012). While Hainline et al. (2016) use both W1–W2 and W2–W3 colours to select BCDs, we omit using W1–W2 colour to select the BCDs since it is used by some authors to select active galactic nuclei (AGN) in dwarf galaxies (Satyapal et al. 2018). Instead, we use bright W4 emission to ensure a high star formation rate for the sample (Lee et al. 2013; Cluver et al. 2017). In Fig. 1, we show the *WISE* colour-colour plot and selection criteria for sources observed with Arecibo Observatory along with sources compiled from literature (see Section 2.2). The Arecibo sample includes only the confirmed BCDs with their spectral energy distribution (SED) indicating no presence of an AGN. Their blue optical morphologies are shown in the optical images from Sloan Digital Sky Survey data release 12 (SDSS DR 12; Alam et al. 2015) in Fig. 2.

2.1.1 Arecibo observations and data reduction

We observed 11 nearby ($z \lesssim 0.03$) MIR-bright BCDs for their HI emission with the Arecibo Telescope during 2012–2013. The observations were taken during two cycles, November–December 2012 and September–December 2013, using standard ON-OFF mode and recording in one-second integrations. Both Arecibo L-band Feed Array (ALFA) and L-band Wide receivers were used. L-band Wide data were taken with the Wide band Arecibo Pulsar Processor (WAPP) spectrometer with 4096 channels across a bandwidth of 50 MHz, giving a velocity resolution of ~ 2.7 km s^{-1} . ALFA data were taken with the spectrometer with 4096 channels across a bandwidth of 100 MHz for a velocity resolution of ~ 5.4 km s^{-1} . The total effective integration time for each source are listed in Table 1.

The data were reduced in IDL using both standard

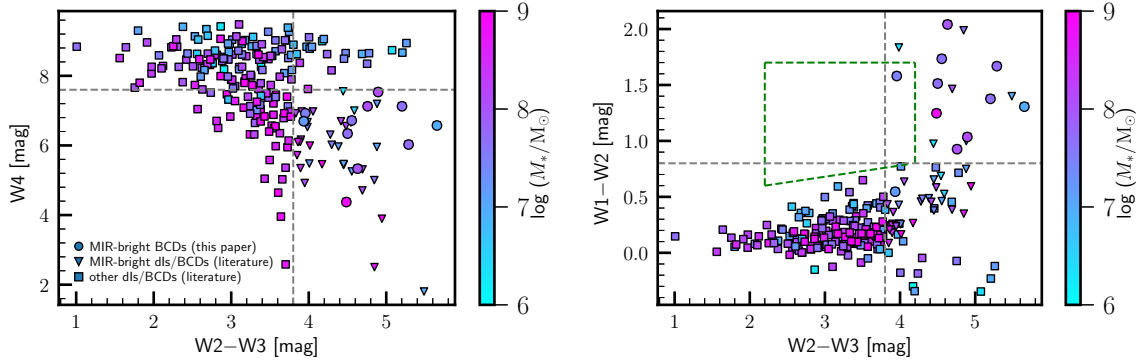


Figure 1. **Left panel:** *WISE* W4 vs W2–W3 for 225 low-redshift starburst dwarf galaxies with data in the AllWISE catalog. MIR-bright BCDs observed with Arecibo are shown with circles. MIR-bright dIs/BCDs and other dIs/BCDs from the literature are shown with downward triangles and squares, respectively. Horizontal and vertical dashed grey lines mark our selection criteria for MIR-bright BCDs. **Right panel:** *WISE* W1–W2 vs W2–W3. Symbols mean same as in the left panel. The dashed vertical grey line represents W2–W3 > 3.8 mag, one of our criteria for selecting MIR-bright BCDs. The dashed horizontal grey line represents the cutoff for selecting AGNs from Stern et al. (2012). The region marked with the dashed green lines represents the AGN selection criteria from Jarrett et al. (2011)

Table 1. Observational details of the Arecibo search during 2012–2013 for HI emission in the BCD sample.

(1) Source	(2) R.A.	(3) Dec.	(4) Date of observation	(5) Observed Central Velocity [km s ⁻¹]	(6) Time observed [s]
W0231+2441	02:31:19.77	+24:41:23.5	2013 Nov. 04	8640	946
W0801+2640	08:01:03.92	+26:40:54.4	2012 Nov. 08,09,11,12,13,14,15	7795	7500
W0830+0225	08:30:44.36	+02:25:55.8	2013 Dec. 13	9450	1499
W1016+3754	10:16:24.50	+37:54:45.8	2012 Dec. 06,07	1170	1200
W1408+1753	14:08:16.24	+17:53:50.7	2013 Sep. 21, 29	7110	2700
W1423+2257	14:23:42.85	+22:57:28.4	2013 Sep. 21, Sep. 29, Oct. 06	9900	2300
W1439+1702	14:39:57.88	+17:02:17.8	2013 Oct. 05,06	9030	2100
W2130+0830	21:30:05.24	+08:30:12.8	2013 Sep. 14,15,16	7800	2338
W2212+2205	22:12:59.35	+22:05:05.6	2013 Sep. 16 Oct.19,25 Dec.08,09	8580	3900
W2238+1400	22:38:31.09	+14:00:27.1	2012 Nov.06,07,08	6176	7550
W2326+0608	23:26:03.58	+06:08:14.9	2013 Dec.08	5010	1100

Notes: Column (1): Source name. Column (2): Right Ascension. Column (3): Declination. Column (4): Date of observation. Column (5): Observed central velocity in km s⁻¹. Column (6): Observation time in seconds. Co-ordinates in this table are from AllWISE catalog (Cutri et al. 2021).

programs provided by the observatory and software developed for combining integrations from multiple observations with ALFA and L-band Wide receiver. Bandpasses were corrected using position switching (ON-OFF)/OFF and Hanning smoothing was applied. Baselines were automatically fit to first order, calibration was applied, and polarizations were averaged. Radio frequency interference (RFI) was identified both automatically and manually and removed from the final spectra. The most common RFI was GPS L3 satellite interference, as many sources in the sample are located near 8500 km s⁻¹. L-band Wide data were smoothed further to align the effective velocity resolution of L-band Wide data with ALFA data at ~ 10 km s⁻¹. Final noise levels vary from 0.2 mJy channel⁻¹ to 0.7 mJy channel⁻¹ (Table 2), though the white noise in several spectra is dominated by baseline structure likely caused by reflections from the blocked aperture of the Arecibo telescope. The parameters, peak flux (S_{peak}), integrated flux (F_{HI}), HI velocity (V_{HI}), and Full Width at

Half Maximum (W_{50}), listed in Table 2, are obtained from HI profiles using standard Arecibo software package *mbmeasure*¹. The uncertainties on these parameters are calculated in the same way as in Koribalski et al. (2004).

2.2 Additional sources from literature

To compare the properties of the 11 BCDs observed with the Arecibo, we collected information on several dIs/BCDs with HI observation from the literature (see references in Tables A1 and A2). Sources with possible contamination by gas-rich galaxy neighbours and HI observations without sufficient spatial resolution have been excluded from our analysis. If multiple HI observations are available, measurements with better sensitivity and resolution are selected. We

¹ <http://www.naic.edu/~rminchin/idl/mbmeasure.pro>

Table 2. Characteristics of HI emission profiles of observed MIR-bright BCDs

(1) Source	(2) V_{opt} [km s ⁻¹]	(3) V_{HI} [km s ⁻¹]	(4) W_{50} [km s ⁻¹]	(5) F_{HI} [mJy km s ⁻¹]	(6) S_{peak} [mJy]	(7) $\Delta S_{\text{rms}} (1\sigma)$ [mJy]	(8) $\log M_{\text{HI}}/M_{\odot}$
W0231+2441	8634	8671±7	42±14	50±40	1.4	0.7	8.3
W0801+0264	7795	7920±5	96±10	222±28	2.4	0.2	8.8
W0830+0225	9443	9413±15	115±30	290±70	2.6	0.5	9.1
W1016+3754	1169	1177±4	61±8	490±60	8.1	0.5	7.5
W1408+1753	7105	-	-	-	-	0.4	< 8.2
W1423+2257	9863	-	-	-	-	0.5	< 8.7
W1439+1702	9024	-	-	-	-	0.5	< 8.3
W2130+0830	7795	-	-	-	-	0.4	< 8.1
W2212+2205	8574	-	-	-	-	0.5	< 8.5
W2238+1400	6176	6165±16	93±32	66±23	0.8	0.2	8.1
W2326+0608	5031	4996±2	99±4	1670±130	18.7	0.5	9.3
W2326+0608*	5031	5023±7	57±15	50±30	1.5	0.4	7.8

*Extended HI disk, here calculated from high resolution GMRT follow-up observations (Chandola et al. 2023).

Notes: Column (1): Source name. Column (2): V_{opt} , velocity corresponding to optical redshift ($c \cdot z$). Column (3): V_{HI} , HI velocity in km s⁻¹ in heliocentric frame. Column (4): W_{50} , velocity width in km s⁻¹ of the profile at 50% of the peak flux level. Column (5): F_{HI} , integrated flux density in mJy km s⁻¹. Column (6): S_{peak} , peak flux density in mJy. Column (7): ΔS_{rms} , noise level per channel in mJy. Column (8): $\log M_{\text{HI}}$, logarithm of the total HI mass in M_{\odot} .

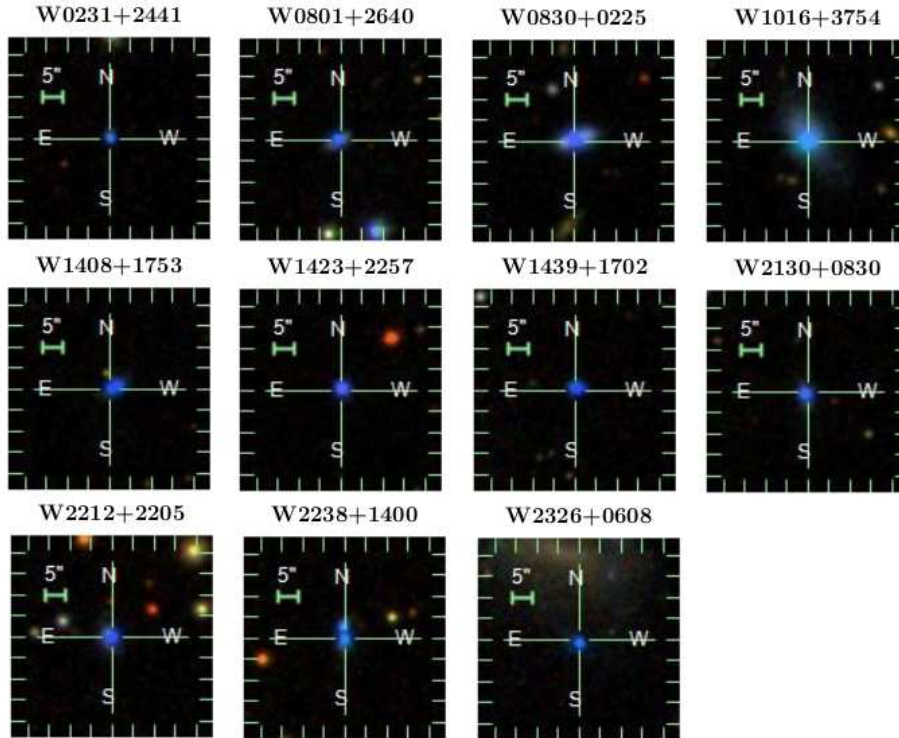


Figure 2. Optical SDSS g , r , i band composite images of the BCDs observed with the Arecibo. The field of view for each of these images is $50'' \times 50''$.

also did not include sources reported with HI non-detections or uncertain detections. This resulted in a sample of additional 297 dIs/BCDs. After including the 11 BCDs observed with the Arecibo telescope, the total number of dIs/BCDs is 308. Although we excluded non-detections from the literature in our analysis due to non-uniform sensitivities, we included non-detections from our observations for completeness purposes, conservatively assuming the upper limit val-

ues as detections. This has no statistically significant effect on our conclusions. Of these 308, we have both stellar masses and star formation rates for 229 sources (also see Section 4). We have based our analysis on these 229 sources. Of these 229, 225 sources have the data in AllWISE and 44 sources, including 11 sources observed with the Arecibo observatory, satisfy our MIR selection criteria. We also use the Arecibo Legacy Fast ALFA (ALFALFA) 100% survey-SDSS

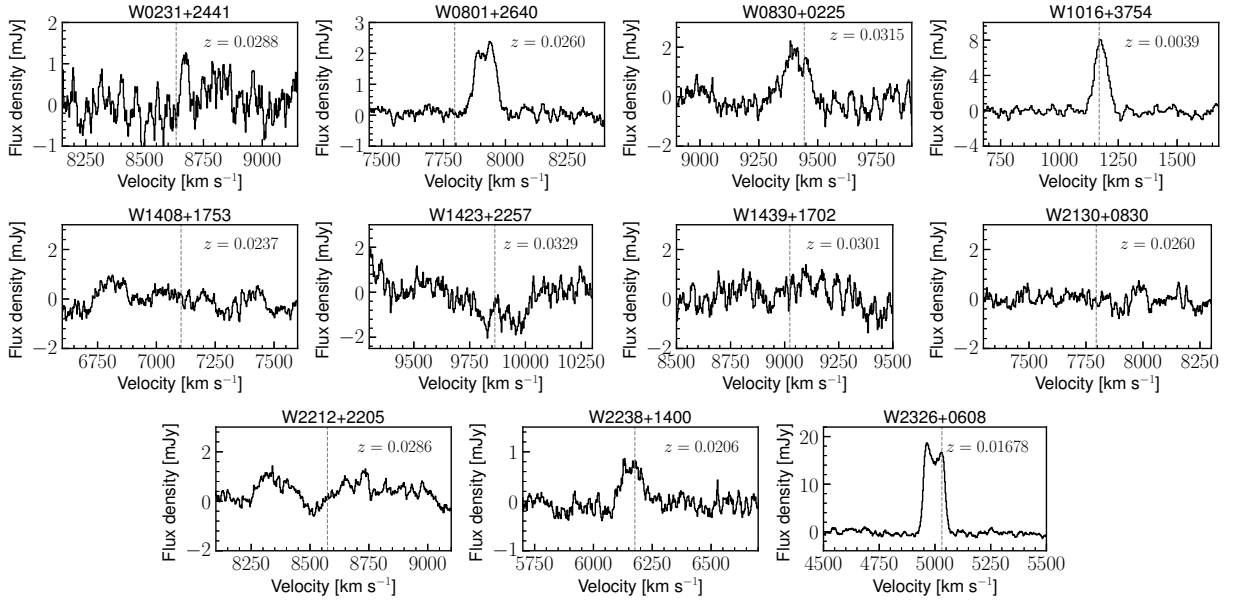


Figure 3. Arecibo HI spectra of the 11 BCDs. Horizontal axes are velocities in the heliocentric frame of rest, and vertical axes are flux densities in mJy. HI is detected in six BCDs: W0231+2441, W0801+2640, W0830+0225, W1016+3754, W2238+1400 and W2326+0608. The optical redshifts are shown at the upper right corner of the spectra. The systemic velocities from optical redshifts are marked with dashed vertical grey lines.

cross-match sample (Durbala et al. 2020), a sample of dwarf galaxies detected in HI by ALFALFA survey (Huang et al. 2012a) and the extended GALEX Arecibo SDSS survey (xGASS, Catinella et al. 2018) for comparison.

3 RESULTS

HI profiles from observations with the Arecibo are shown in Figure 3. We detect HI in six out of eleven sources in the sample. Of the six detections, four sources, W0801+0264, W0830+0225, W1016+3754, W2326+0608, have peak flux (S_{peak}) above 5σ significance. W2238+1400, has a 4σ detection and W0231+2441 has a marginal detection (2σ). HI mass has been calculated using the equation from Roberts (1975)

$$M_{\text{HI}} \sim 2.36 \times 10^5 \times \left(\frac{D_L}{\text{Mpc}} \right)^2 \times \left(\frac{F_{\text{HI}}}{\text{Jy km s}^{-1}} \right) M_{\odot}, \quad (1)$$

where D_L is the luminosity distance and

$$F_{\text{HI}} = \int \frac{S(v)}{\text{Jy}} \frac{dv}{\text{km s}^{-1}} \quad (2)$$

is the integrated flux over the velocity range where the HI line has been detected. As it is difficult to find a good distance estimator for these compact galaxies we have used luminosity distance for most of the sources. However, we have used the distances estimated using the tip of the red giant branch (TRGB; Lee et al. 1993) or Tully-Fisher (TF; Tully & Fisher 1977) method for the nearby sources ($c^*z \lesssim 500 \text{ km s}^{-1}$) where it is available in the literature. The median HI mass is $10^{8.3} M_{\odot}$.

The upper limit to the HI mass was calculated assuming a 5σ detection of a single peak boxcar spectral profile with

velocity width at half peak flux of 50 km s^{-1} :

$$M_{\text{HI}} \sim 2.36 \times 10^5 \times \left(\frac{D_L}{\text{Mpc}} \right)^2 \times 5 \Delta S_{\text{rms}} \Delta v \sqrt{\frac{50}{\Delta v}} M_{\odot}, \quad (3)$$

where Δv is the velocity resolution in km s^{-1} (10 km s^{-1}) and ΔS_{rms} is the noise level per channel in Jy. The upper HI mass limit for three sources (W1408+1753, W1423+2257, W2212+2205) was calculated using larger “effective” noise levels (0.6 mJy, 1.0 mJy, 0.8 mJy, respectively) than reported in Table 2 because of significant baseline structure present near the expected location of the source. The median upper limit on HI mass for the non-detections is also estimated to be $10^{8.3} M_{\odot}$.

W1016+3754 was previously observed in HI by Pustilnik & Martin (2007) using the Nancay Radio Telescope (NRT), though the HI profile experienced confusion with neighbouring galaxy UGC 5540 in the large Nancay beam. Pustilnik & Martin (2007) derived HI mass of $\log(M_{\text{HI}}/M_{\odot}) = 7.9$ for W1016+3754. We obtain a slightly lower HI mass of $\log(M_{\text{HI}}/M_{\odot}) = 7.5$ after resolving the object with Arecibo. W2238+1400 was previously observed for HI emission by Pustilnik & Martin (2007) with NRT and Filho et al. (2013) with Effelsberg without a detection. We detect HI after over two hours of integration with Arecibo. Of the six detections, two sources (W0801+2640, W2326+0608) have double horn profile shapes while the other four (W0231+2441, W0830+0225, W1016+3754, W2238+1400) have single component profiles. W2326+0608 has a neighbouring galaxy that could not be resolved with the Arecibo beam. From high-resolution GMRT observations towards W2326+0608, we find dense ($\gtrsim 10^{21} \text{ cm}^{-2}$) HI gas near the BCD (Chandola et al. 2023). The parameters reported from GMRT which we use in our analysis, are also provided in Table 2.

Previous literature has noted that there is often a large

amount of HI gas outside the optical disk and the dwarf galaxies show a larger fraction of gas outside the optical disk (Wang et al. 2014, 2016, 2020; Hunt et al. 2020). For our sample, it is impossible to locate the HI gas due to our limited spatial resolution. Hence, we use the global HI mass for our study. This could create a bias if massive galaxies have less gas outside the optical disk than less massive galaxies. To check this, we follow the approach taken by Hunt et al. (2020). We find that the optical-to-HI radius ratio and the ratio of HI mass outside the optical disk to total HI mass do not change systematically with stellar mass for our sample, implying that the sample is unbiased (see Section A1).

4 STELLAR MASS (M_*) AND STAR FORMATION RATES (SFR)

To estimate the properties of the dIs/BCDs, we assembled the multi-band photometric data from *Galaxy Evolution Explorer* (GALEX; Bianchi et al. 2017), Panoramic Survey Telescope and Rapid Response System (Pan-STARRS; Flewelling et al. 2020), SDSS (Alam et al. 2015), Two Micron All Sky Survey (2MASS; Skrutskie et al. 2006), UKIRT Infrared Deep Sky Survey (UKIDSS; Lawrence et al. 2007) and AllWISE (Cutri et al. 2021) to construct the UV to Infrared spectral energy distribution (SED). We used a cross-match radius of 5 arcseconds around SDSS/Pan-STARRS optical coordinates to obtain photometric data points for the SED. To decompose the stellar components in the host galaxy, we use the method of Assef et al. (2008, 2010) in which the SED of a galaxy is described by the linear contribution of empirical spectral templates (Assef et al. 2010). The three empirical SED templates – an elliptical galaxy (E), a spiral galaxy (Sbc), and an irregular galaxy (Im) – are used to model the SED of the host galaxy in the wavelength range 0.03–30 μm (Assef et al. 2010). The E, Sbc and Im templates represent components of an old stellar population, a continuously star-forming population and a starburst population, respectively.

4.1 Stellar masses

Based on the best model for each SED, we derived the K-correction. Then using the correlations between rest frame *ugriz* colours and M/L ratios reported by Bell et al. (2003), we estimated the stellar mass-to-light ratio for the host galaxies. Using this method, we obtained stellar mass estimates for 214 sources. We compared the stellar mass of sources common in GALEX-SDSS-WISE Legacy Catalog (GSWLC, Salim et al. 2016, 2018) and our compilation of dIs/BCDs using M/L from Bell et al. (2003). We have 28 sources common in both samples with no troublesome photometry in GSWLC. As Bell et al. (2003) consider a relatively smooth star-forming history and have higher estimates of M/L (Zibetti et al. 2009), we find stellar mass estimates are slightly larger by ~ 0.1 dex compared to the method used by Salim et al. (2016, 2018). For another 11 sources, we obtained stellar masses from the SDSS MPA-JHU database (Brinchmann et al. 2004a)² where stellar masses were de-

rived using fits to the SDSS photometry. For another four sources, we use values from the literature (see the references in Tables A1 and A2).

4.2 SFRs and sSFRs

Considering extinction from dust in the host galaxies, we correct the GALEX FUV and NUV luminosity using the WISE W4, and estimate the extinction-corrected SFR using the method of Hao et al. (2011) and Kennicutt & Evans (2012). We estimate the extinction-corrected FUV/NUV SFR for 148 galaxies. For another 21 galaxies, where the FUV/NUV fluxes are not available from GALEX, we predict the FUV luminosities using the model SED fitting and correct for extinction using the W4 values.

Some BCDs are young starburst galaxies with little or no dust extinction (Wu et al. 2007). For 53 such sources, where there is no clear detection in the WISE W4 band, we use FUV/NUV SFR without correcting for dust extinction. For another 5 sources, we use the SFR from MPA-JHU catalog (Brinchmann et al. 2004a)³ where the SFR with corrections for dust attenuation were derived using the methods of Brinchmann et al. (2004b) and aperture corrections were applied using the methodology of Salim et al. (2007). For 2 additional galaxies, we obtained values from the literature.

In Fig. 4, we plot star formation rate (SFR) versus stellar mass (M_*) for the sample of 229 dIs/BCDs (44 MIR-bright dIs/BCDs). SFRs and sSFRs for MIR-bright dIs/BCDs are ~ 10 times higher than typical values for other dIs/BCDs of similar stellar masses. The median SFR is $10^{-0.74} M_\odot \text{ yr}^{-1}$ for MIR-bright BCDs as compared to $10^{-1.46} M_\odot \text{ yr}^{-1}$ for other dIs/BCDs. The median sSFR values are $\sim 10^{-8.6} \text{ yr}^{-1}$ and $\sim 10^{-9.5} \text{ yr}^{-1}$ for MIR-bright and other dIs/BCDs, respectively. We also show fits to main sequence star-forming galaxies ($M_* > 10^{10} M_\odot$) at $z = 0$ (Renzini & Peng 2015), $z = 1$ and $z = 6$ (Popesso et al. 2023) in Fig. 4. The median sSFR ($10^{-7.8} \text{ yr}^{-1}$) for MIR-bright BCDs observed with Arecibo is higher (sSFR $> 10^{-8} \text{ yr}^{-1}$) than main sequence star-forming galaxies at $z = 6$. In the fundamental formation relation (FFR; Dou et al. 2021a,b), sSFR can be expressed as

$$\text{sSFR} = f_{\text{HI}} \times \text{SFE} \quad (4)$$

where $f_{\text{HI}} = M_{\text{HI}}/M_*$ is the gas fraction or HI mass to stellar mass ratio and SFE is the star formation efficiency of the gas. SFE is given by the equation

$$\text{SFE} = \frac{\text{SFR}}{M_{\text{HI}}} = \frac{1}{\tau_{\text{HI}}} \quad (5)$$

where τ_{HI} is the atomic gas depletion timescale. The high sSFR for these objects could be due to higher gas fractions or higher star formation efficiencies (lower depletion timescales) of the atomic HI gas, or both. Table 3 reports the median values of M_* , sSFR, f_{HI} and τ_{HI} for different subsamples of M_* and sSFR. Table 4 reports the Spearman's correlation coefficients of f_{HI} and τ_{HI} relation with M_* and sSFR. In the next section, we discuss the HI mass to stellar mass ratio and gas depletion timescale of these galaxies to understand their high sSFRs.

² <http://wwwmpa.mpa-garching.mpg.de/SDSS/DR7/Data/stellarmass.html> <http://wwwmpa.mpa-garching.mpg.de/SDSS/DR7/sfrs.html>

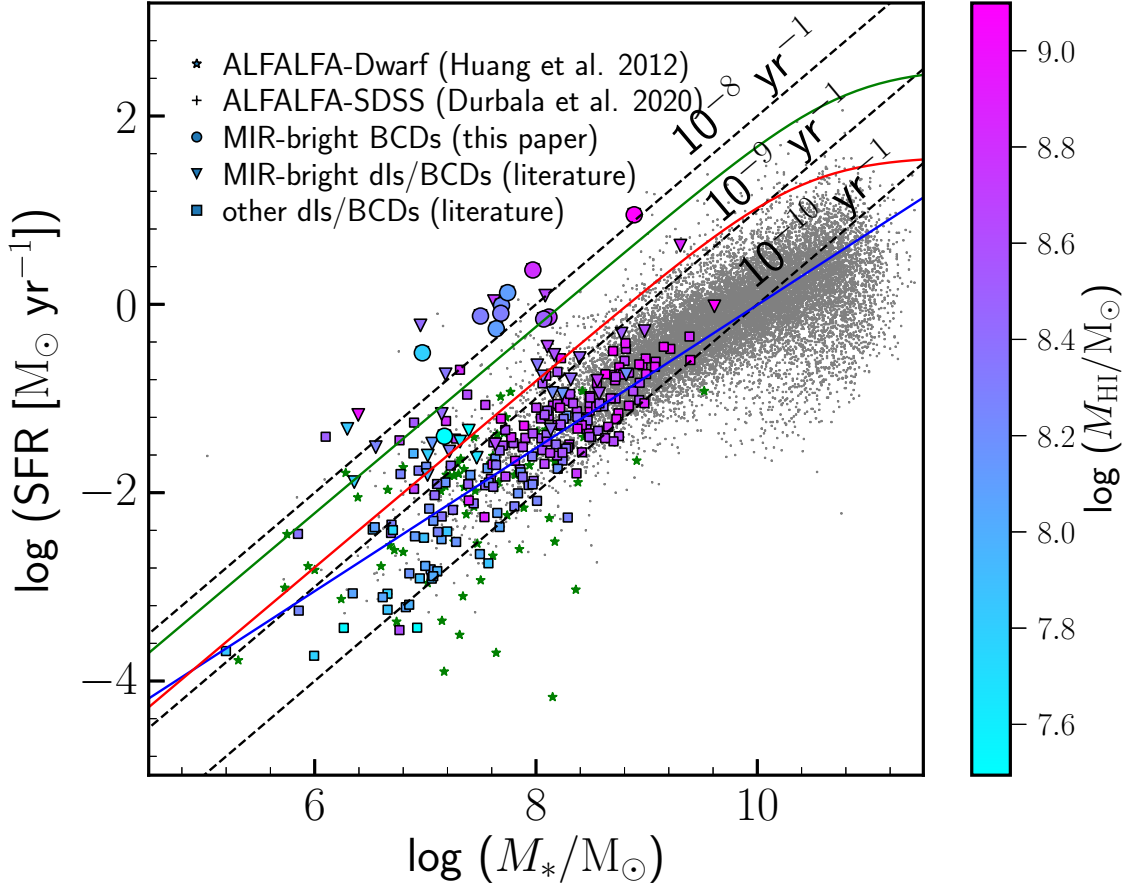


Figure 4. SFR vs M_* . Different symbols mean the same as in Fig. 1. The colour scale shows the HI mass of the dIs/BCDs. The solid lines in blue, red and green colours show fits to the main sequence star-forming galaxies at $z=0$ (Renzini & Peng 2015), 1 and 6 (Popesso et al. 2023), respectively. Dashed diagonal lines in black show different sSFR levels. Most of the BCDs observed with the Arecibo have their sSFRs higher than the main sequence star-forming galaxies at $z=0$. Data from ALFALFA(100 %)-SDSS survey (Durbala et al. 2020) is also shown in grey coloured ‘+’ symbols. Stellar masses for the ALFALFA-SDSS sample were derived using the method of Taylor et al. (2011). SFRs were derived from *GALEX* NUV luminosities corrected for extinction using MIR 22 μm (Durbala et al. 2020). ALFALFA dwarf galaxies (Huang et al. 2012a) are also shown in green.

5 ANALYSIS AND DISCUSSION

5.1 HI mass to stellar mass ratio ($f_{\text{HI}} = M_{\text{HI}}/M_*$)

Fig. 5 shows f_{HI} vs. M_* and f_{HI} vs. sSFR for all subsamples mentioned earlier. The f_{HI} values vary between ~ 0.01 and 1000 for different stellar masses of these sources. Median f_{HI} values are $10^{0.5 \pm 0.4}$ (~ 3.2) and $10^{0.3 \pm 0.4}$ (~ 2.0) for MIR-bright and other dIs/BCDs, respectively. The median f_{HI} for the Arecibo observed sample is $10^{0.5 \pm 0.2}$ (~ 3.2). The f_{HI} vs. M_* plot in panel (a) shows a negative correlation between the two parameters for all subsamples. f_{HI} increases gradually with decreasing M_* , which is consistent with the findings of Catinella et al. (2018). This suggests that the baryonic mass is dominated by cold atomic gas at lower stellar masses. This anti-correlation is stronger for higher sSFR ($>10^{-8.5} \text{ yr}^{-1}$) dIs/BCDs as compared to lower sSFR dIs/BCDs ($<10^{-8.5} \text{ yr}^{-1}$). At lower stellar masses ($<10^{7.5} M_{\odot}$) dIs/BCDs with higher sSFR have higher gas fractions. MIR-bright as well as the other dIs/BCDs follow the same relation implying there is no difference in the baryonic com-

position of MIR-bright and other dIs/BCDs at a given stellar mass.

Large area shallow HI surveys such as ALFALFA are biased towards the gas-rich galaxies of different stellar masses due to their sensitivity limitation, and hence we see a higher density of ALFALFA-SDSS sources towards the higher values of f_{HI} in f_{HI} vs. M_* relation. This is not the case for targeted samples selected based on optical criteria where gas-poor sources are also detected with M_{HI}/M_* ratio up to $\sim 2\%$ (Catinella et al. 2018). The median f_{HI} for local star-forming main sequence galaxies with an average stellar mass of $10^{9.14}$ from xGASS sample (Catinella et al. 2018) is ~ 0.8 . This is a factor of 3 lower than the median values for dIs/BCDs in the local universe, implying a strong dependence of f_{HI} on stellar mass. From stacking star-forming galaxies at an average redshift of ~ 1.0 , a recent study by Chowdhury et al. (2022) finds that f_{HI} is ~ 1.4 . Hence, dIs/BCDs in the local universe have higher f_{HI} than the $z \sim 1$ star-forming main sequence massive galaxies ($>10^9 M_{\odot}$) as well.

Fig. 5 (b) shows f_{HI} as function of sSFR. For both types

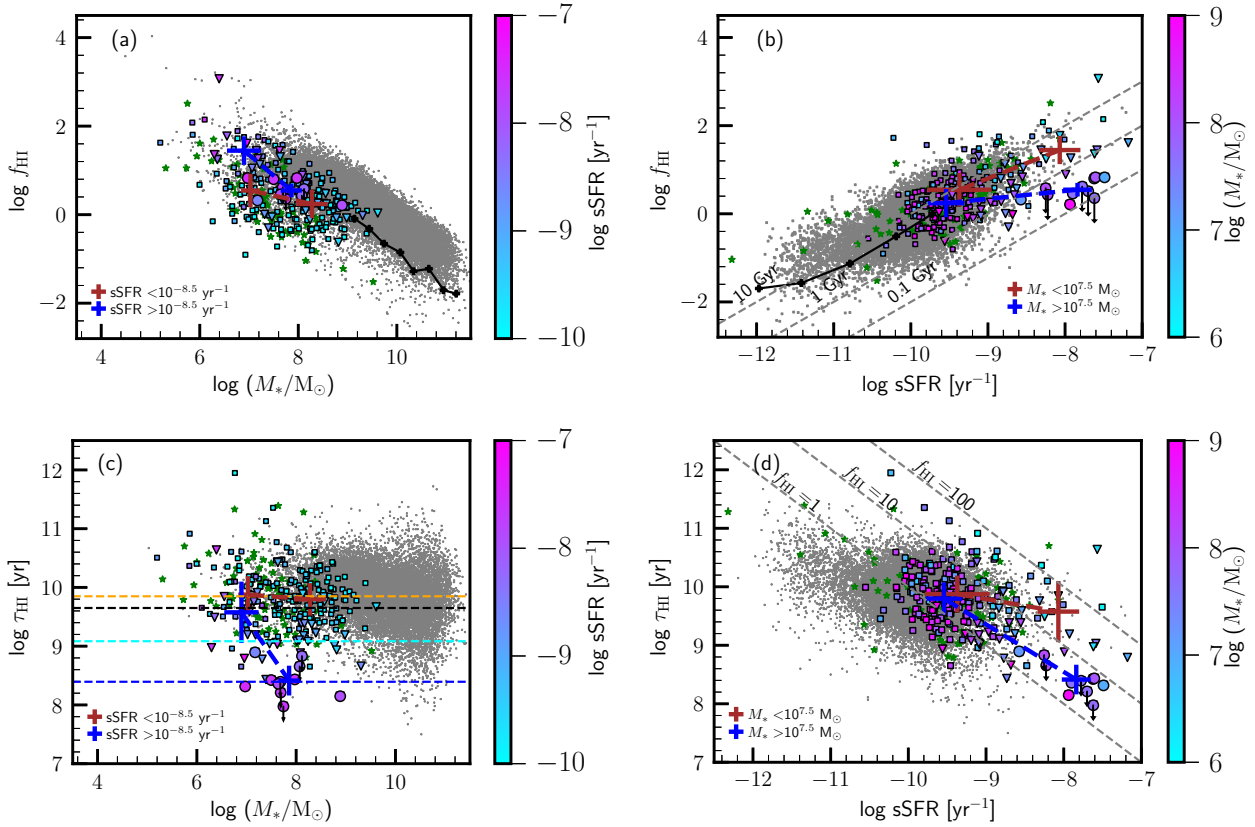


Figure 5. (a) f_{HI} vs. M_* for all subsamples of dIs/BCDs. Symbols are the same as in Fig. 4. Median values of f_{HI} for different subsamples of stellar masses and sSFR are shown with blue (sSFR $> 10^{-8.5} \text{ yr}^{-1}$) and brown (sSFR $\leq 10^{-8.5} \text{ yr}^{-1}$) colour error bars. (b) f_{HI} vs. sSFR. Median values of f_{HI} for different subsamples of stellar masses and sSFR are shown with blue ($M_* > 10^{7.5} M_\odot$) and brown ($M_* \leq 10^{7.5} M_\odot$) colour error bars. Dashed diagonal grey lines show the depletion timescales. In plots (a) and (b) median f_{HI} for xGASS galaxies (Catinella et al. 2018) are shown in black colour. (c) Gas depletion timescale (τ_{HI}) vs. M_* . Dashed horizontal lines represent the median of τ_{HI} for other dIs/BCDs in orange, all MIR-bright dIs/BCDs in cyan and MIR-bright BCDs observed with the Arecibo observatory in blue. Black dashed horizontal line represents the median τ_{HI} for local main sequence galaxies ($M_* > 10^9 M_\odot$) from Saintonge et al. (2017) and Catinella et al. (2018). Median values of τ_{HI} for different subsamples of stellar masses and sSFR are shown with blue (sSFR $> 10^{-8.5} \text{ yr}^{-1}$) and brown (sSFR $\leq 10^{-8.5} \text{ yr}^{-1}$) colour error bars. (d) τ_{HI} vs. sSFR. Median values of τ_{HI} for different subsamples of stellar masses and sSFR are shown in blue ($M_* > 10^{7.5} M_\odot$) and brown ($M_* \leq 10^{7.5} M_\odot$) colour error bars. The dashed grey diagonal lines represent different levels of f_{HI} . For $f_{\text{HI}} = 1$, the depletion time scale is equal to the e-folding time scale. In plots (a) and (c) colour scales show sSFR, while in plots (b) and (d) it shows the stellar masses.

Table 3. Median values of M_* , sSFR, f_{HI} and τ_{HI} for different subsamples of M_* and sSFR.

M_* category	sSFR category	Median log M_* [M_\odot]	Median log sSFR [yr^{-1}]	Median log f_{HI}	Median log τ_{HI} [yr]	N^\dagger
low ($\leq 10^{7.5} M_\odot$)	low ($\leq 10^{-8.5} \text{ yr}^{-1}$)	7.0 ± 0.2	-9.4 ± 0.4	0.5 ± 0.4	9.9 ± 0.3	58
low ($\leq 10^{7.5} M_\odot$)	high ($> 10^{-8.5} \text{ yr}^{-1}$)	6.9 ± 0.3	-8.1 ± 0.3	1.4 ± 0.3	9.6 ± 0.5	17
high ($> 10^{7.5} M_\odot$)	low ($\leq 10^{-8.5} \text{ yr}^{-1}$)	8.3 ± 0.3	-9.5 ± 0.2	0.2 ± 0.3	9.8 ± 0.3	144
high ($> 10^{7.5} M_\odot$)	high ($> 10^{-8.5} \text{ yr}^{-1}$)	7.9 ± 0.2	-7.8 ± 0.2	0.5 ± 0.2	8.4 ± 0.3	10

† Number of sources.

of dIs/BCDs, the f_{HI} increases with increasing sSFR. However, at higher sSFR ($> 10^{-8.5} \text{ yr}^{-1}$) there is scatter in f_{HI} due to different stellar masses. The dIs/BCDs with lower stellar masses have a higher median f_{HI} ($10^{1.4 \pm 0.3}$). The dIs/BCDs with higher sSFR and higher stellar masses appears to diverge from the f_{HI} -sSFR relation towards lower median f_{HI} ($10^{0.5 \pm 0.2}$). The MIR-bright BCDs observed with the Arecibo have the lower f_{HI} as compared to the

dIs/BCDs of similar sSFR studied in the literature. This implies less fuel per unit stellar mass is available for a similar star-formation rate per unit stellar mass and hence, a lesser role of f_{HI} in the current starburst episode.

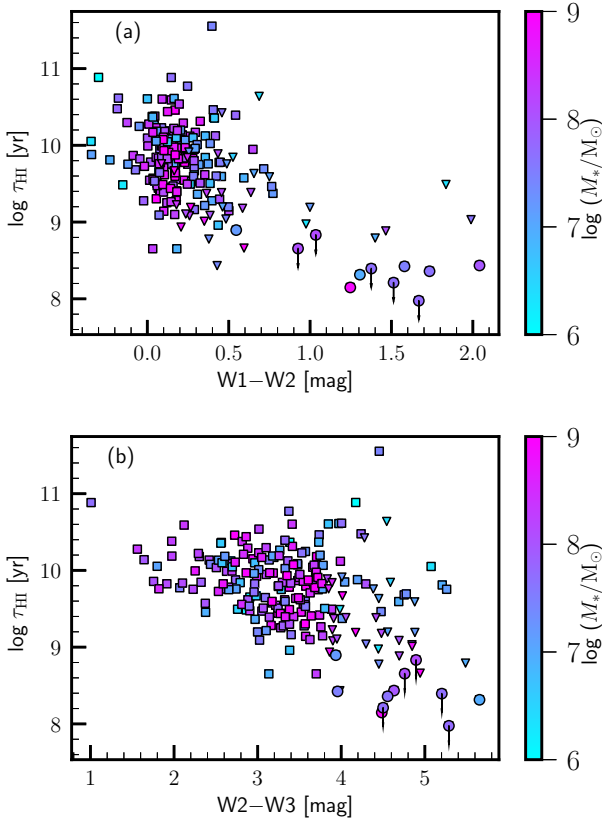


Figure 6. τ_{HI} vs *WISE* W1–W2 and *WISE* W2–W3 in panels (a) and (b) respectively. Symbols mean the same as in Fig. 1. The Arecibo-observed BCDs with young starburst ($\text{sSFR} \gtrsim 10^{-8.5} \text{ yr}^{-1}$) and low depletion time scales show very red W1–W2 and W2–W3 colours.

Table 4. Spearman’s correlation coefficients (R-value) of f_{HI} and τ_{HI} relation with M_* and sSFR for different subsamples of M_* and sSFR.

Subsample	X-axis	Y-axis	R-value	p-value	N [†]
$\text{sSFR} \leq 10^{-8.5} \text{ yr}^{-1}$	M_*	f_{HI}	−0.4	1.1×10^{-09}	202
$\text{sSFR} > 10^{-8.5} \text{ yr}^{-1}$	M_*	f_{HI}	−0.73	0.0021	27
$\text{sSFR} \leq 10^{-8.5} \text{ yr}^{-1}$	M_*	τ_{HI}	−0.13	0.06	202
$\text{sSFR} > 10^{-8.5} \text{ yr}^{-1}$	M_*	τ_{HI}	−0.63	0.012	27
$M_* \leq 10^{7.5} M_{\odot}$	sSFR	f_{HI}	0.63	3.3×10^{-5}	75
$M_* > 10^{7.5} M_{\odot}$	sSFR	f_{HI}	0.56	4.34×10^{-17}	154
$M_* \leq 10^{7.5} M_{\odot}$	sSFR	τ_{HI}	−0.34	0.04	75
$M_* > 10^{7.5} M_{\odot}$	sSFR	τ_{HI}	−0.41	2.5×10^{-9}	154

[†]Number of sources.

5.2 Atomic HI gas depletion timescales

Cold neutral gas is considered the fuel reservoir for star formation activity, and the global HI content of galaxies is related to how long the current star formation activity can be supported. We estimate the HI gas depletion time scale (τ_{HI}) using

$$\tau_{\text{HI}} = \frac{1}{\text{SFE}} = \frac{M_{\text{HI}}}{\text{SFR}} = \frac{f_{\text{HI}}}{\text{sSFR}}. \quad (6)$$

The median τ_{HI} for MIR-bright and other dIs/BCDs are $10^{9.1 \pm 0.4} \text{ yr}$ ($\sim 1.3 \text{ Gyr}$) and $10^{9.8 \pm 0.3} \text{ yr}$ ($\sim 6.3 \text{ Gyr}$), respec-

tively. At the current SFR, MIR-bright dIs/BCDs will run out of their fuel earlier than other dIs/BCDs. We find the median HI atomic gas depletion timescales for the sample of MIR-bright and other dIs/BCDs are ~ 0.26 and ~ 1.26 times $\sim 5 \text{ Gyr}$, the gas depletion time scales of higher stellar mass main sequence galaxies (Saintonge et al. 2017). If we only consider the BCDs observed with the Arecibo, the median τ_{HI} is estimated to be $10^{8.4 \pm 0.2} \text{ yrs}$ or $\sim 0.3 \text{ Gyr}$ (conservatively assuming the upper limits as detections). This is lower than $\sim 0.6 \text{ Gyr}$ reported for relatively higher redshift Green Pea galaxies (Kanekar et al. 2021). This is more than an order of magnitude ($\sim 3.9 \sigma$) lower than other dIs/BCDs. This is also lower than $\sim 1.7 \text{ Gyr}$, the depletion timescale for high redshift main sequence galaxies ($z \sim 1$; Chowdhury et al. 2022).

We examine the dependence of τ_{HI} on M_* and sSFR in the bottom panels of Fig. 5. It appears that there is no significant correlation (Spearman’s R-value of -0.08 , p-value of 0.21) between τ_{HI} and M_* for the combined sample of dIs/BCDs (Fig. 5c). There is a dispersion in the relation because lower sSFR ($< 10^{-8.5} \text{ yr}^{-1}$) galaxies have higher depletion timescales at higher stellar masses. Dividing the sample into lower and higher sSFR strengthens the anti-correlation (Spearman’s R-value: -0.63 , p-value: 0.01) for higher sSFR objects. Fig. 5(d) also shows a weak but significant negative correlation of τ_{HI} with sSFR (Spearman’s R value: -0.38 , p-value: 2.7×10^{-9}). Again in this relation, there is a dispersion due to lower mass galaxies having higher τ_{HI} at higher sSFR ($> 10^{-8.5} \text{ yr}^{-1}$). There is stronger τ_{HI} -sSFR anti-correlation (R-value: -0.41 , p-value: 2.5×10^{-9}) for galaxies with higher stellar mass ($> 10^{7.5} M_{\odot}$). MIR-bright dIs/BCDs from the Arecibo observations cover the highest sSFR and lowest τ_{HI} region.

In the literature, almost no dependence of τ_{HI} on M_* was found by Saintonge et al. (2017) for relatively higher mass galaxies ($> 10^9 M_{\odot}$) and Thuan et al. (2016) for low stellar mass ($\gtrsim 10^5 M_{\odot}$) and low metallicity ($< 1/10 Z_{\odot}$) BCDs. However, HI selected samples from the ALFALFA survey (Haynes et al. 2011) find that the depletion time scale decreases or star-formation efficiency, $\text{SFE} = 1/\tau_{\text{HI}}$, increases with stellar mass (Huang et al. 2012a,b; Jaskot et al. 2015), albeit subject to considerable scatter in τ_{HI} at lower stellar masses. Surveys like ALFALFA are likely to detect more HI rich but optically faint objects compared to optically selected samples, and hence objects with higher depletion time scale (lower SFE) are only detected at low stellar masses (Huang et al. 2012a,b). Recently, Hunt et al. (2020) found that τ_{HI} shows inverse relation with sSFR. Compared to Huang et al. (2012b), Jaskot et al. (2015) and Hunt et al. (2020), we explored higher sSFR regimes and find a much stronger anti-correlation of τ_{HI} with M_* for higher sSFR, and with sSFR for higher stellar mass dwarf galaxies.

An almost constant atomic gas depletion timescale with M_* and the sSFR may imply a balance between the gas accretion from intergalactic medium (IGM) and its conversion to molecular gas and finally to stars is regulated by external mechanisms (Schiminovich et al. 2010). In some earlier studies with optically selected samples, while atomic gas depletion timescales were found to be almost constant with M_* and sSFR, molecular gas depletion timescales were found to vary with M_* and sSFR, differing by more than an order of magnitude with atomic gas depletion timescales

for lower stellar masses and high sSFRs (Hunt et al. 2015; Saintonge et al. 2017). These results were interpreted as a large fraction of HI gas being not directly related to the star-formation process in these systems (Saintonge et al. 2017). Contrary to this, an inverse relation may imply a relatively larger fraction of HI gas being actively involved in the current high star-burst episode. Since most of the sources have depletion timescales larger than $1/\text{sSFR}$, it should be possible to sustain the current SFR to at least double the stellar mass.

5.3 Why does the Arecibo sample has the highest specific star formation rate or lowest depletion timescale?

As mentioned earlier in the previous section, the high sSFR or starburst nature of the galaxies depends mainly on two factors: (1) the gas fraction (f_{HI} or availability of HI gas per unit stellar mass), and (2) SFE or SFR per unit mass of HI gas. For the starburst dIs/BCDs with $\text{sSFR} > 10^{-8.5} \text{ yr}^{-1}$, the role of f_{HI} or τ_{HI} in the current high starburst episode is strongly dependent on their stellar masses. At the lower stellar masses, it is mainly f_{HI} which drives the starburst, while for higher stellar masses it is mainly SFE of the gas. Based on their stellar masses, f_{HI} of the MIR-bright BCDs in the Arecibo sample are similar to the other low sSFR dIs/BCDs in the literature. Hence, it is mainly the low gas depletion time scales or high SFE of the gas which drives the high sSFR or current starburst episode. In this subsection, we discuss the reason for the high depletion time scale in these systems. Many compact starburst BCDs with warm dust can be detected using *WISE* colours (Hainline et al. 2016). Hence, we plot the sample of dIs/BCDs in τ_{HI} vs *WISE* colour plots (Fig 6a and Fig 6b). Galaxies with lower depletion timescale have the redder W1–W2 and W2–W3 colours. The sources in the Arecibo sample have the reddest W1–W2 colours, indicating the presence of warm dust. In the sample of 11 BCDs observed with Arecibo, we find that 10 BCDs have $W1-W2 > 0.8$. Note that this red colour is not due to active galactic nuclei (AGN), which have higher luminosities (Hainline et al. 2016). Among all dIs/BCDs, 16 sources satisfy this criterion. The median HI depletion time scale for the dIs/BCDs with red W1–W2 colours is ~ 0.46 Gyr. BCDs with redder W1–W2 colours are known to have larger $H\alpha$ equivalents widths (EQW), $H\alpha$ luminosities and ionizing photon rates (Hainline et al. 2016). The similar gas fraction (f_{HI}) at a given stellar mass suggests that despite the high ionizing photon rate there is no change in the baryonic composition of the Arecibo sample. This could be due to the high star-forming gas density shielding HI gas from ionization (Hirashita & Hunt 2004). This high density of gas could also create the favourable conditions for faster conversion of HI to H_2 (Krumholz et al. 2009). Hence, the very low depletion timescale or high star-formation efficiency for BCDs with $W1-W2 > 0.8$ could be the result of runaway star-formation in dense, dust-rich and compact super star clusters, similar to what is seen in SBS 033–052, resulting in heated dust and low depletion timescales or high specific star-formation rates (Hirashita & Hunt 2004).

6 SUMMARY AND CONCLUSION

In this paper, we present Arecibo HI 21 cm observations of 11 MIR-bright BCDs, six of which resulted in detection. We further combine these results with dIs/BCDs in the literature and compare properties of MIR-bright dIs/BCDs with dIs/BCDs that are not MIR-bright. We have the following conclusions from our study:

- MIR-bright dIs/BCDs follow the same HI mass-stellar mass relation as other dIs/BCDs, showing HI to stellar mass ratio decreasing with stellar mass and implying a similar gas-dominated baryonic composition. We find that the $f_{\text{HI}}-M_*$ relation shows stronger anti-correlation at higher sSFR ($> 10^{-8.5} \text{ yr}^{-1}$) implying that the current starburst episode in lower mass galaxies is mainly due to the higher gas fractions. In comparison to dI/BCDs of similar sSFR in the literature, our sample of BCDs observed with the Arecibo telescope has higher stellar mass and hence lower HI gas to stellar mass ratio, implying a lesser role of f_{HI} in the current starburst episode.
- We find a significant and strong anti-correlation of gas depletion timescales (τ_{HI}) with M_* in high sSFR ($> 10^{-8.5} \text{ yr}^{-1}$) dIs/BCDs and with sSFR in the sample of higher stellar mass ($> 10^{7.5} M_{\odot}$) objects. Strong $\tau_{\text{HI}}-\text{sSFR}$ and $\tau_{\text{HI}}-M_*$ anti-correlation indicates a more significant role of star-formation efficiency (SFE) in higher stellar mass and higher sSFR dIs/BCDs. This could imply a larger fraction of HI gas being actively involved in star formation. MIR-bright dIs/BCDs have shorter gas depletion timescales or higher star formation efficiencies as compared to the other dIs/BCDs, especially BCDs observed with the Arecibo have median depletion timescale of ~ 0.3 Gyr, less by one order of magnitude compared to the median depletion time scale, ~ 6.3 Gyr for other dIs/BCDs.
- For the sources with $W1-W2 > 0.8$, HI depletion timescale are very low, ~ 0.46 Gyr. Compared to other dIs/BCDs from the literature, BCDs in the Arecibo sample have the reddest W1–W2 colours. The majority of the BCDs in the Arecibo sample satisfy the criterion $W1-W2 > 0.8$ implying the presence of warm dust. BCDs with redder W1–W2 colours are known to have high ionizing photon rates and compact starburst regions. However, the HI gas fraction for the Arecibo sample is similar to the other dIs/BCDs of similar stellar mass in literature, implying no change in the baryonic composition due to ionizing photons. This could be due to the dense star-forming gas shielding the atomic HI gas from excessive ionization and creating physical conditions favourable for faster HI to H_2 conversion. Hence the high star formation efficiency or low depletion time scales are possibly due to the compact, dense and dust-rich star forming super clusters resulting in high sSFR.

Future HI surveys with SKA pathfinder telescopes like Five hundred metre Aperture radio Telescope (FAST; Nan et al. 2011; Li & Pan 2016; Li et al. 2018), will probe larger numbers of galaxies with similarly high sSFR, and will provide definitive tests of the results found here, many of which are marginal or just hinted at. With larger sky coverage and better HI sensitivity than those of Arecibo (Zhang et al. 2019), FAST can probe BCDs of lower stellar masses and higher sSFR. Such a sample will shed significant light on the char-

acteristics of BCDs, particularly, their star formation history.

ACKNOWLEDGEMENTS

We thank an anonymous reviewer for useful comments which helped to improve the paper significantly. This work is supported by the National Natural Science Foundation of China (NSFC) Grant No. 11988101, No. 12050410259, No. 11550110181, No. 11725313, No. 12041302, the International Partnership Program of Chinese Academy of Sciences grant No. 114A11KYSB20160008. YC was sponsored by the Chinese Academy of Sciences Visiting Fellowship for Researchers from Developing Countries, Grant No. 2013FFJB0009, by the FAST distinguished young researcher fellowship (19-FAST-02) from the Center for Astronomical Mega-Science, CAS, and Ministry of Science and Technology (MOST) grant no. QNJ2021061003L. Y.P. acknowledge National Science Foundation of China (NSFC) Grant No. 12125301, 12192220, and 12192222, and the science research grants from the China Manned Space Project with NO. CMS-CSST-2021-A07. YZM acknowledges the support of the National Research Foundation with Grant No. 150580, No. 120385, and No. 120378. Portions of this research were carried out at the Jet Propulsion Laboratory, California Institute of Technology, under a contract with the National Aeronautics and Space Administration.

We thank the staff of Arecibo Observatory (AO) which made these observations possible. During 2011-2018, the AO was operated by SRI International under a cooperative agreement with the National Science Foundation (AST-1100968), and in alliance with Ana G. Méndez-Universidad Metropolitana, and the Universities Space Research Association. Currently, the AO is a facility of the National Science Foundation operated under cooperative agreement (AST-1744119) by the University of Central Florida in alliance with Universidad Ana G. Méndez (UAGM) and Yang Enterprises (YEI), Inc. YC thanks Priyadarshini Bangale for helping with the script to improve one of the figures. This work has also used different Python packages e.g. NUMPY, ASTROPY, SCIPY and MATPLOTLIB. We thank numerous contributors for these packages. This research has made use of the SIMBAD database, operated at CDS, Strasbourg, France. This research has made use of the VizieR catalogue access tool, CDS, Strasbourg, France (DOI : 10.26093/cds/vizieR). The original description of the VizieR service was published in 2000, A&AS 143, 23

This publication makes use of data products from the *Wide-Field Infrared Survey Explorer*, which is a joint project of the University of California, Los Angeles, and the Jet Propulsion Laboratory, California Institute of Technology, funded by the National Aeronautics and Space Administration.

This publication makes use of data products from the Two Micron All Sky Survey, which is a joint project of the University of Massachusetts and the Infrared Processing and Analysis Center/California Institute of Technology, funded by the National Aeronautics and Space Administration and the National Science Foundation.

This work also makes use of Sloan Digital Sky Survey (SDSS)-III. Funding for SDSS-III has been provided by

the Alfred P. Sloan Foundation, the Participating Institutions, the National Science Foundation and the US Department of Energy Office of Science. The SDSS-III web site is <http://www.sdss3.org/>. SDSS-III is managed by the Astrophysical Research Consortium for the Participating Institutions of the SDSS-III Collaboration including the University of Arizona, the Brazilian Participation Group, Brookhaven National Laboratory, Carnegie Mellon University, University of Florida, the French Participation Group, the German Participation Group, Harvard University, the Instituto de Astrofísica de Canarias, the Michigan State/Notre Dame/JINA Participation Group, Johns Hopkins University, Lawrence Berkeley National Laboratory, Max Planck Institute for Astrophysics, Max Planck Institute for Extraterrestrial Physics, New Mexico State University, New York University, Ohio State University, Pennsylvania State University, University of Portsmouth, Princeton University, the Spanish Participation Group, University of Tokyo, University of Utah, Vanderbilt University, University of Virginia, University of Washington and Yale University.

This work also makes use of data products from the Panoramic Survey Telescope and Rapid Response System (Pan-STARRS). The Pan-STARRS1 Surveys were made possible through contributions by the Institute for Astronomy, the University of Hawaii, the Pan-STARRS Project Office, the Max-Planck Society and its participating institutes, the Max Planck Institute for Astronomy, Heidelberg and the Max Planck Institute for Extraterrestrial Physics, Garching, The Johns Hopkins University, Durham University, the University of Edinburgh, the Queen's University Belfast, the Harvard-Smithsonian Center for Astrophysics, the Las Cumbres Observatory Global Telescope Network Incorporated, the National Central University of Taiwan, the Space Telescope Science Institute, and the National Aeronautics and Space Administration under Grant No. NNX08AR22G issued through the Planetary Science Division of the NASA Science Mission Directorate, the National Science Foundation Grant No. AST-1238877, the University of Maryland, Eotvos Lorand University (ELTE), and the Los Alamos National Laboratory. The Pan-STARRS1 Surveys are archived at the Space Telescope Science Institute (STScI) and can be accessed through MAST, the Mikulski Archive for Space Telescopes. Additional support for the Pan-STARRS1 public science archive is provided by the Gordon and Betty Moore Foundation.

DATA AVAILABILITY

HI 21-cm data from the Arecibo observations can be accessed using proposal ID A2715 at <https://www.naic.edu/datacatalog/>. Multi-band photometric data for UV (GALEX), optical (Pan-STARRS, SDSS), and infrared (2MASS, UKIDSS and AllWISE) are publicly available and can be accessed using VizieR catalogue service <https://vizier.cds.unistra.fr/viz-bin/VizieR>. The data from Huang et al. (2012a) (J/AJ/143/133) and Durbala et al. (2020) (J/AJ/160/271) are also publicly available and can be accessed using VizieR catalogue service. Stellar masses and star formation rates from MPA-JHU group are also publicly available at

<http://wwwmpa.mpa-garching.mpg.de/SDSS/DR7/Data/stellarmass.html>,
and <http://wwwmpa.mpa-garching.mpg.de/SDSS/DR7/sfrs.html>.

REFERENCES

- Adams E. A. K., Oosterloo T. A., 2018, *A&A*, **612**, A26
 Alam S., et al., 2015, *ApJS*, **219**, 12
 Amorín R. O., Pérez-Montero E., Vílchez J. M., 2010, *ApJ*, **715**, L128
 Ashley T., Simpson C. E., Elmegreen B. G., Johnson M., Pokhrel N. R., 2017, *AJ*, **153**, 132
 Assef R. J., et al., 2008, *ApJ*, **676**, 286
 Assef R. J., et al., 2010, *ApJ*, **713**, 970
 Bell E. F., McIntosh D. H., Katz N., Weinberg M. D., 2003, *ApJS*, **149**, 289
 Bianchi L., Shiao B., Thilker D., 2017, *ApJS*, **230**, 24
 Bravo-Alfaro H., Brinks E., Baker A. J., Walter F., Kunth D., 2004, *AJ*, **127**, 264
 Brinchmann J., Charlot S., Heckman T. M., Kauffmann G., Tremonti C., White S. D. M., 2004a, ArXiv Astrophysics e-prints,
 Brinchmann J., Charlot S., White S. D. M., Tremonti C., Kauffmann G., Heckman T., Brinkmann J., 2004b, *MNRAS*, **351**, 1151
 Catinella B., et al., 2018, *MNRAS*, **476**, 875
 Chandola Y., Tsai C. W., Li D., Sengupta C., Ma Y. Z., Zuo P., 2023, *MNRAS*, **523**, 3848
 Chengalur J. N., Pustilnik S. A., Martin J. M., Kniazev A. Y., 2006, *MNRAS*, **371**, 1849
 Chengalur J. N., Pustilnik S. A., Egorova E. S., 2017, *MNRAS*, **465**, 2342
 Chowdhury A., Kanekar N., Chengalur J. N., 2022, *ApJ*, **937**, 103
 Cluver M. E., Jarrett T. H., Dale D. A., Smith J. D. T., August T., Brown M. J. I., 2017, *ApJ*, **850**, 68
 Comte G., Petrosian A. R., Ohanian G. A., Stepanian J. A., 1999, *Astrophysics*, **42**, 149
 Cutri R. M., et al., 2021, VizieR Online Data Catalog, p. II/328
 Dale D. A., Helou G., Neugebauer G., Soifer B. T., Frayer D. T., Condon J. J., 2001, *AJ*, **122**, 1736
 Donoso E., et al., 2012, *ApJ*, **748**, 80
 Dou J., et al., 2021a, *ApJ*, **907**, 114
 Dou J., et al., 2021b, *ApJ*, **915**, 94
 Durbala A., Finn R. A., Crone Odekon M., Haynes M. P., Koopmann R. A., O'Donoghue A. A., 2020, *AJ*, **160**, 271
 Ekta B., Chengalur J. N., 2010, *MNRAS*, **403**, 295
 Ekta Chengalur J. N., Pustilnik S. A., 2006, *MNRAS*, **372**, 853
 Ekta Chengalur J. N., Pustilnik S. A., 2008, *MNRAS*, **391**, 881
 Ekta B., Pustilnik S. A., Chengalur J. N., 2009, *MNRAS*, **397**, 963
 Filho M. E., et al., 2013, *A&A*, **558**, A18
 Flewelling H. A., et al., 2020, *ApJS*, **251**, 7
 Gawiser E., et al., 2007, *ApJ*, **671**, 278
 Gil de Paz A., Madore B. F., Pevunova O., 2003, *ApJS*, **147**, 29
 Griffith R. L., et al., 2011, *ApJ*, **736**, L22
 Guseva N. G., Izotov Y. I., Fricke K. J., Henkel C., 2017, *A&A*, **599**, A65
 Hainline K. N., Reines A. E., Greene J. E., Stern D., 2016, *ApJ*, **832**, 119
 Hao C.-N., Kennicutt R. C., Johnson B. D., Calzetti D., Dale D. A., Moustakas J., 2011, *ApJ*, **741**, 124
 Haynes M. P., et al., 2011, *AJ*, **142**, 170
 Hirashita H., Hunt L. K., 2004, *A&A*, **421**, 555
 Hirschauer A. S., et al., 2016, *ApJ*, **822**, 108
 Hsyu T., Cooke R. J., Prochaska J. X., Bolte M., 2018, *ApJ*, **863**, 134
 Huang M.-L., Kauffmann G., 2014, *MNRAS*, **443**, 1329
 Huang S., Haynes M. P., Giovanelli R., Brinchmann J., Stierwalt S., Neff S. G., 2012a, *AJ*, **143**, 133
 Haynes M. P., Giovanelli R., Brinchmann J., 2012b, *ApJ*, **756**, 113
 Huchtmeier W. K., Gopal-Krishna Petrosian A., 2005, *A&A*, **434**, 887
 Huchtmeier W. K., Petrosian A., Gopal-Krishna Kunth D., 2007, *A&A*, **462**, 919
 Hunt L. K., et al., 2015, *A&A*, **583**, A114
 Hunt L. K., Tortora C., Ginolfi M., Schneider R., 2020, *A&A*, **643**, A180
 Hunter D. A., Hoffman L., 1999, *AJ*, **117**, 2789
 Izotov Y. I., Thuan T. X., Guseva N. G., 2012, *A&A*, **546**, A122
 Izotov Y. I., Thuan T. X., Guseva N. G., Liss S. E., 2018, *MNRAS*, **473**, 1956
 Jaiswal S., Omar A., 2020, *MNRAS*, **498**, 4745
 James B. L., Koposov S., Stark D. P., Belokurov V., Pettini M., Olszewski E. W., 2015, *MNRAS*, **448**, 2687
 Jarrett T. H., et al., 2011, *ApJ*, **735**, 112
 Jaskot A. E., Oey M. S., Salzer J. J., Van Sistine A., Bell E. F., Haynes M. P., 2015, *ApJ*, **808**, 66
 Kanekar N., Ghosh T., Rhoads J., Malhotra S., Harish S., Chengalur J. N., Jones K. M., 2021, *ApJ*, **913**, L15
 Kennicutt R. C., Evans N. J., 2012, *ARA&A*, **50**, 531
 Kniazev A. Y., Grebel E. K., Hao L., Strauss M. A., Brinkmann J., Fukugita M., 2003, *ApJ*, **593**, L73
 Koribalski B. S., et al., 2004, *AJ*, **128**, 16
 Krumholz M. R., McKee C. F., Tumlinson J., 2009, *ApJ*, **693**, 216
 Kunth D., 1999, *Ap&SS*, **265**, 489
 Lawrence A., et al., 2007, *MNRAS*, **379**, 1599
 Lee M. G., Freedman W. L., Madore B. F., 1993, *ApJ*, **417**, 553
 Lee J. C., Hwang H. S., Ko J., 2013, *ApJ*, **774**, 62
 Lelli F., Verheijen M., Fraternali F., 2014a, *MNRAS*, **445**, 1694
 Lelli F., Verheijen M., Fraternali F., 2014b, *A&A*, **566**, A71
 Li D., Pan Z., 2016, *Radio Science*, **51**, 1060
 Li D., et al., 2018, *IEEE Microwave Magazine*, **19**, 112
 McCall M. L., Vaduvescu O., Pozo Nunez F., Barr Dominguez A., Fingerhut R., Unda-Sanzana E., Li B., Albrecht M., 2012, *A&A*, **540**, A49
 Morales-Luis A. B., Sánchez Almeida J., Aguerri J. A. L., Muñoz-Tuñón C., 2011, *ApJ*, **743**, 77
 Nan R., et al., 2011, *International Journal of Modern Physics D*, **20**, 989
 Paswan A., Omar A., Jaiswal S., 2018, *MNRAS*, **473**, 4566
 Popesso P., et al., 2023, *MNRAS*, **519**, 1526
 Pustilnik S. A., Martin J. M., 2007, *A&A*, **464**, 859
 Pustilnik S. A., Brinks E., Thuan T. X., Lipovetsky V. A., Izotov Y. I., 2001, *AJ*, **121**, 1413
 Ramya S., Kantharia N. G., Prabhu T. P., 2011, *ApJ*, **728**, 124
 Renzini A., Peng Y.-j., 2015, *ApJ*, **801**, L29
 Roberts M. S., 1975, Radio Observations of Neutral Hydrogen in Galaxies. the University of Chicago Press, p. 309
 Roychowdhury S., Chengalur J. N., Chiboucas K., Karachentsev I. D., Tully R. B., Kaisin S. S., 2012, *MNRAS*, **426**, 665
 Sabbi E., et al., 2018, *ApJS*, **235**, 23
 Saintonge A., et al., 2011, *MNRAS*, **415**, 61
 Saintonge A., et al., 2017, *ApJS*, **233**, 22
 Salim S., et al., 2007, *ApJS*, **173**, 267
 Salim S., et al., 2016, *ApJS*, **227**, 2
 Salim S., Boquien M., Lee J. C., 2018, *ApJ*, **859**, 11
 Salzer J. J., Rosenberg J. L., Weisstein E. W., Mazzarella J. M., Bothun G. D., 2002, *AJ*, **124**, 191
 Sánchez Almeida J., Pérez-Montero E., Morales-Luis A. B., Muñoz-Tuñón C., García-Benito R., Nuza S. E., Kitauro F. S., 2016, *ApJ*, **819**, 110
 Sánchez Almeida J., Filho M. E., Dalla Vecchia C., Skillman E. D., 2017, *ApJ*, **835**, 159
 Satyapal S., Abel N. P., Secrest N. J., 2018, *ApJ*, **858**, 38
 Schiminovich D., et al., 2010, *MNRAS*, **408**, 919
 Skrutskie M. F., et al., 2006, *AJ*, **131**, 1163

- Stern D., et al., 2012, *ApJ*, **753**, 30
 Taylor E. N., et al., 2011, *MNRAS*, **418**, 1587
 Teich Y. G., et al., 2016, *ApJ*, **832**, 85
 Thuan T. X., Martin G. E., 1981, *ApJ*, **247**, 823
 Thuan T. X., Lipovetsky V. A., Martin J.-M., Pustilnik S. A., 1999, *A&AS*, **139**, 1
 Thuan T. X., Hibbard J. E., Lévrier F., 2004, *AJ*, **128**, 617
 Thuan T. X., Goehring K. M., Hibbard J. E., Izotov Y. I., Hunt L. K., 2016, *MNRAS*, **463**, 4268
 Tsai C.-W., et al., 2012, in American Astronomical Society Meeting Abstracts #219. p. 201.03
 Tully R. B., Fisher J. R., 1977, *A&A*, **54**, 661
 Tully R. B., Rizzi L., Shaya E. J., Courtois H. M., Makarov D. I., Jacobs B. A., 2009, *AJ*, **138**, 323
 Tully R. B., et al., 2013, *AJ*, **146**, 86
 Wang J., et al., 2014, *MNRAS*, **441**, 2159
 Wang J., Koribalski B. S., Serra P., van der Hulst T., Roychowdhury S., Kamphuis P., Chengalur J. N., 2016, *MNRAS*, **460**, 2143
 Wang J., Catinella B., Saintonge A., Pan Z., Serra P., Shao L., 2020, *ApJ*, **890**, 63
 Wright E. L., et al., 2010, *AJ*, **140**, 1868
 Wu Y., Charmandaris V., Hao L., Brandl B. R., Bernard-Salas J., Spoon H. W. W., Houck J. R., 2006, *ApJ*, **639**, 157
 Wu Y., et al., 2007, *ApJ*, **662**, 952
 Yang H., Malhotra S., Rhoads J. E., Wang J., 2017, *ApJ*, **847**, 38
 Zhang K., et al., 2019, *Science China Physics, Mechanics, and Astronomy*, **62**, 959506
 Zibetti S., Charlot S., Rix H.-W., 2009, *MNRAS*, **400**, 1181
 Zwicky F., 1966, *ApJ*, **143**, 192

APPENDIX A:

A1 The location of HI gas

Several previous studies found that HI gas has a larger extent than the optical disk of galaxies (Wang et al. 2014, 2016, 2020; Hunt et al. 2020). For our study, it is important to check whether the HI measurement is coming from a similar HI distribution relative to the optical disk. Fig. A1 (upper panel) shows the variation of optical-to-H I disk radius ratio versus stellar mass for our sample. HI disk radius (R_{HI}) is the semi-major axis of isophote where the HI gas column density is $1 \text{ M}_{\odot} \text{ pc}^{-2}$, and estimated it using the HI mass-size relation from Wang et al. (2016). We used optical major axis values from the SIMBAD database to estimate the R_{opt} for 168 sources. We find that the optical-to-HI radius ratio does not vary with stellar mass and has a median value of ~ 0.27 . In Fig A1 (lower panel), we follow Wang et al. (2016) and Hunt et al. (2020) to predict the HI mass outside the optical radius, $M_{\text{HI}}(\text{out, prediction})$. We find that the ratio of $M_{\text{HI}}(\text{out, prediction})$ to M_{HI} does not systematically depend on stellar mass. The median logarithmic value of $M_{\text{HI}}(\text{out, prediction})/M_{\text{HI}}$ is ~ -0.11 , implying $\sim 78\%$ of HI gas is outside the stellar disk.

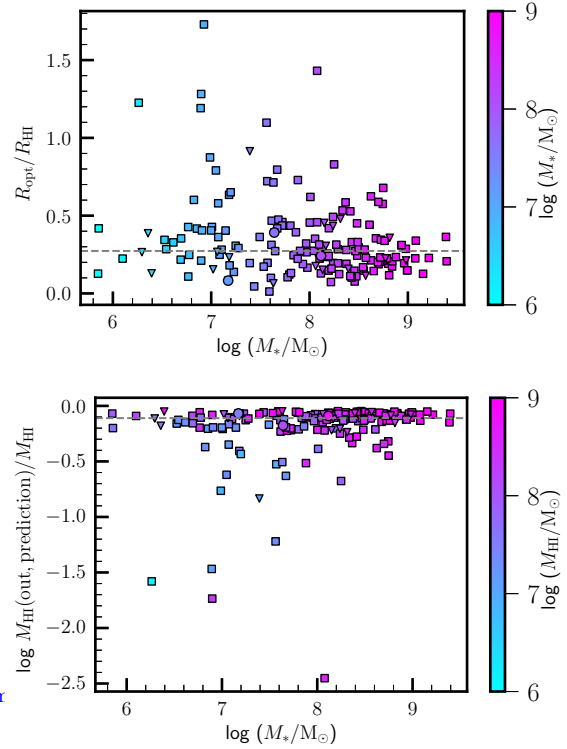


Figure A1. **Top panel:** $R_{\text{opt}}/R_{\text{HI}}$ vs M_* . The symbols mean the same as in Fig. 6. The horizontal grey dashed line shows the median value of $R_{\text{opt}}/R_{\text{HI}}$. **Bottom panel:** $M_{\text{HI}}(\text{out, prediction})/M_{\text{HI}}$ vs M_* . The horizontal grey dashed line shows the median value of $\log(M_{\text{HI}}(\text{out, prediction})/M_{\text{HI}})$.

Table A1. Sample of 44 MIR-bright dIs/BCDs.

(1) Source	(2) Redshift	(3) log $M(\text{HI})$ (Ref.) [M_{\odot}]	(4) telescope	(5) log SFR (ref.) [$M_{\odot} \text{ yr}^{-1}$]	(6) log M_{*} (ref.) [M_{\odot}]	(7) log sSFR [yr^{-1}]	(8) log f_{HI}	(9) log τ_{HI} [yr]
0122+0743, UGC 993	0.00975	9.47 (1)	NRT	-1.17 (1)	6.39 (1)	-7.57	3.07	10.64
W0231+2441	0.0288	8.30 (2)	Arecibo	-0.12 (2)	7.50 (2)	-7.62	0.80	8.42
0335-052	0.01349	8.98 (3)	NRT	0.03 (2)	7.62 (2)	-7.59	1.45	9.03
II Zw 40	0.00267	8.36 (4)	Arecibo	-0.22 (3)	6.96 (2)	-7.18	1.61	8.79
0749+568	0.0183	8.90 (3)	NRT	-0.45 (2)	8.10 (2)	-8.55	0.83	9.39
W0801+2640	0.026	8.80 (2)	Arecibo	0.36 (2)	7.97 (2)	-7.61	0.83	8.43
W0830+0225	0.0315	9.10 (2)	Arecibo	0.95 (2)	8.89 (2)	-7.94	0.21	8.15
Mrk 108	0.00477	8.20 (5)	GMRT	-0.95 (2)	8.24 (2)	-9.19	-0.11	9.08
Mrk 22	0.00539	8.57 (6)	GMRT	-1.33 (2)	8.13 (2)	-9.46	0.43	9.89
W1016+3754	0.0039	7.50 (2)	Arecibo	-1.40 (2)	7.17 (2)	-8.57	0.32	8.90
Mrk 140	0.00556	8.77 (7)	GBT	-0.95 (2)	8.57 (2)	-9.52	0.24	9.76
SBS 1037+494	0.00518	8.28 (8)	Effelsberg	-1.52 (2)	6.55 (2)	-8.07	1.77	9.84
Mrk 724	0.00406	6.96 (4)	Arecibo	-1.34 (2)	7.39 (2)	-8.73	-0.30	8.43
J1044+0353	0.01315	8.40 (9)	GBT	-0.74 (2)	7.18 (2)	-7.93	1.27	9.19
Haro 3	0.00314	8.73 (7)	GBT	-0.31 (4)	8.77 (2)	-9.08	-0.07	9.01
Mrk 1446	0.00988	8.54 (8)	Effelsberg	-0.80 (2)	8.31 (2)	-9.11	0.26	9.37
Wa 22	0.00472	8.83 (4)	Arecibo	-1.49 (2)	7.63 (2)	-9.12	1.31	10.42
UM 439	0.00368	8.40 (4)	Arecibo	-1.16 (2)	7.15 (2)	-8.31	1.45	9.76
Mrk 1450	0.00311	7.30 (8)	Effelsberg	-1.46 (3)	7.31 (2)	-8.77	0.01	8.78
Mrk 750	0.00252	7.42 (4)	Arecibo	-1.61 (3)	7.02 (2)	-8.63	0.57	9.20
UM 461	0.00350	8.04 (10)	NRT	-1.48 (2)	7.06 (2)	-8.54	1.05	9.59
1152+579	0.01726	8.95 (3)	NRT	0.09 (2)	8.08 (2)	-7.99	0.89	8.88
J1201+0211	0.00327	7.18 (9)	GBT	-1.89 (2)	6.36 (2)	-8.25	1.24	9.49
J1202+5415	0.01055	7.79 (9)	GBT	-1.32 (3)	6.29 (3)	-7.62	1.36	8.97
Haro 06	0.00673	8.54 (4)	Arecibo	-0.57 (2)	8.40 (2)	-8.97	0.26	9.23
Mrk 49	0.00510	8.30 (4)	Arecibo	-0.65 (4)	8.01 (2)	-8.66	0.43	9.09
Wa 53	0.00865	8.16 (4)	Arecibo	-0.94 (2)	8.15 (2)	-9.09	0.09	9.18
I Zw 36	0.00094	7.82 (11)	VLA	-1.81 (2)	7.02 (2)	-8.83	0.80	9.63
CG 184	0.00313	8.30 (4)	Arecibo	-1.56 (3)	7.22 (2)	-8.78	1.13	9.91
Wa 69	0.0147	8.78 (4)	Arecibo	-0.54 (2)	8.17 (2)	-8.70	0.68	9.38
Mrk 67	0.0032	7.41 (4)	Arecibo	-1.63 (2)	7.46 (2)	-9.09	-0.05	9.04
Mrk 1369	0.01194	8.86 (4)	Arecibo	-0.28 (2)	8.98 (2)	-9.27	-0.08	9.19
W1408+1759	0.0237	<8.20 (2)	Arecibo	-0.01 (2)	7.69 (2)	-7.70	0.51	8.21
W1423+2257	0.0329	<8.70 (2)	Arecibo	-0.14 (2)	8.12 (2)	-8.25	0.58	8.83
SBS 1428+457	0.00782	9.01 (8)	Effelsberg	-0.81 (3)	8.55 (2)	-9.37	0.47	9.84
W1439+1702	0.0301	<8.30 (2)	Arecibo	-0.10 (2)	7.68 (2)	-7.78	0.62	8.39
II Zw 070	0.00401	8.36 (4)	Arecibo	-0.77 (2)	8.06 (2)	-8.83	0.28	9.11
1629+205	0.01719	9.25 (3)	NRT	0.62 (2)	9.30 (2)	-8.68	-0.02	8.66
Mrk 1499	0.00897	8.18 (8)	Effelsberg	-0.74 (3)	8.81 (2)	-9.56	-0.63	8.93
2116+020, Mrk 513	0.01818	9.58 (3)	NRT	-0.02 (2)	9.61 (2)	-9.63	0.04	9.67
W2130+0830	0.026	<8.10 (2)	Arecibo	0.12 (2)	7.74 (2)	-7.62	0.36	7.98
W2212+2205	0.0286	<8.50 (2)	Arecibo	-0.16 (2)	8.07 (2)	-8.23	0.43	8.66
W2238+1400	0.0206	8.10 (2)	Arecibo	-0.26 (2)	7.64 (2)	-7.90	0.46	8.36
W2326+0608	0.01678	7.80 (13)	GMRT	-0.52 (3)	6.97 (2)	-7.49	0.83	8.31

Notes: Different columns are as follows: (1) Source name, (2) redshift (3) logarithmic value of $M(\text{HI})$ in units of M_{\odot} , (4) telescope used, columns (5) to (9) are logarithmic values for star formation rate (SFR), stellar mass (M_{*}), specific star formation rate (sSFR), ratio of HI mass to stellar mass (f_{HI}) and depletion time scale τ_{HI} .

References for HI mass: (1) Pustilnik & Martin (2007), (2) This paper, (3) Thuan et al. (1999), (4) Salzer et al. (2002), (5) Ramya et al. (2011), (6) Paswan et al. (2018), (7) Thuan & Martin (1981), (8) Huchtmeier et al. (2005), (9) Thuan et al. (2016), (10) Comte et al. (1999) (11) Lelli et al. (2014b), (12) Huchtmeier et al. (2007), (13) Chandola et al. (2023).

References for star formation rates: (1) MPA-JHU SDSS DR 7 catalog, (2) Estimated using FUV luminosity corrected for dust extinction using W4 values, (3) Using predicted FUV luminosity from SED fitting and corrected for dust extinction using W4 values, (4) Estimated using NUV luminosity corrected for dust extinction using W4 values.

References for stellar mass: (1) MPA-JHU SDSS DR 7 catalog, (2) this paper, (3) Thuan et al. (2016).

All redshifts are from SIMBAD database except for those reported with HI in this paper which are from Zhang Ludan et al. in preparation. HI masses from the literature are re-estimated according to the cosmological luminosity distances except for the sources from Lelli et al. (2014b) where the distances are estimated using tip of the red giant branch (TRGB) method. Abbreviations for different telescope names mean as follows: NRT: Nancay Radio Telescope, GBT: Green Bank Telescope, GMRT: Giant Metrewave Radio Telescope, VLA: Very Large Array

Table A2. Sample of other 185 dIs/BCDs detected with HI from the literature.

Source	Redshift	log $M(\text{HI})$ (ref.) [M_{\odot}]	telescope	log SFR (ref.) [$M_{\odot} \text{ yr}^{-1}$]	log M_* (ref.) [M_{\odot}]	log sSFR [yr^{-1}]	log f_{HI}	log τ_{HI} [yr]
AGC 748778	0.00086	6.67 (1)	VLA	-3.73 (1)	6.00 (1)	-9.73	0.68	10.40
0012-018, Mrk 546	0.01311	8.68 (2)	NRT	-0.60 (2)	8.80 (1)	-9.40	-0.12	9.28
J0015+0104	0.00685	8.49 (3)	Effelsberg	-3.46 (3)	6.77 (1)	-10.23	1.72	11.95
UM 241	0.01409	8.80 (4)	Arecibo	-0.75 (2)	8.70 (1)	-9.45	0.09	9.55
UM 38	0.00463	8.40 (4)	Arecibo	-1.47 (2)	7.79 (1)	-9.27	0.61	9.88
UM 40	0.00449	8.80 (4)	Arecibo	-1.49 (2)	8.30 (1)	-9.79	0.50	10.29
J0031-0934,LEDA 989253	0.01132	8.65 (5)	GBT	-1.83 (1)	7.72 (1)	-9.55	0.92	10.48
UM 51	0.01412	9.25 (4)	Arecibo	-1.16 (1)	8.74 (1)	-9.90	0.50	10.40
UM 69	0.00655	9.07 (4)	Arecibo	-1.08 (2)	8.84 (1)	-9.92	0.23	10.15
UM 80	0.01610	9.25 (4)	Arecibo	-1.13 (1)	8.48 (1)	-9.61	0.76	10.38
0111+075, Mrk 564	0.01848	9.15 (2)	NRT	-0.65 (4)	8.96 (1)	-9.61	0.19	9.80
UM 92	0.02309	8.64 (4)	Arecibo	-1.14 (1)	8.37 (1)	-9.50	0.27	9.77
UM 330	0.017	8.73 (4)	Arecibo	-1.03 (1)	8.28 (1)	-9.31	0.45	9.75
UM 336	0.01924	8.94 (4)	Arecibo	-1.29 (1)	8.22 (1)	-9.51	0.71	10.23
J0133+1342	0.00867	7.83 (5)	GBT	-1.77 (4)	6.94 (1)	-8.71	0.89	9.59
UM 345	0.01891	9.31 (4)	Arecibo	-0.97 (2)	8.49 (1)	-9.46	0.83	10.29
AGC 110482	0.00119	7.28 (1)	VLA	-3.22 (1)	6.82 (1)	-10.04	0.46	10.50
UM 372, UGC 1297	0.00569	8.80 (4)	Arecibo	-1.79 (4)	8.37 (1)	-10.16	0.43	10.59
AGC 111977	0.00069	6.85 (1)	VLA	-2.75 (5)	7.57 (2)	-10.32	-0.72	9.60
UM 408	0.01172	8.87 (4)	Arecibo	-1.08 (2)	8.15 (1)	-9.23	0.72	9.95
UM 417	0.00926	8.21 (4)	Arecibo	-1.47 (2)	7.62 (1)	-9.08	0.60	9.68
Mrk 370	0.00252	8.63 (4)	Arecibo	-1.32 (4)	8.46 (1)	-9.78	0.18	9.96
Mrk 600	0.00338	8.56 (4)	Arecibo	-1.51 (2)	7.88 (1)	-9.40	0.68	10.07
UGC 3672A	0.00329	8.65 (6)	GMRT	-1.96 (1)	6.90 (1)	-8.86	1.75	10.61
NGC 2366	0.00034	8.79 (7)	VLA	-1.57 (1)	8.41 (3)	-9.99	0.37	10.36
AGC 174585	0.00119	6.90 (1)	VLA	-2.91 (5)	6.95 (2)	-9.86	-0.05	9.81
AGC 174605	0.00117	7.27 (1)	VLA	-3.07 (1)	6.34 (1)	-9.41	0.93	10.34
HS 0822+3542	0.00269	7.93 (8)	GMRT	-2.44 (2)	5.85 (1)	-8.29	2.08	10.37
J0843+4025	0.00207	6.68 (5)	GBT	-2.88 (1)	6.66 (1)	-9.73	0.02	9.75
0846+3522	0.00831	7.48 (9)	NRT	-1.89 (4)	7.18 (1)	-9.07	0.30	9.37
AGC 182595	0.00133	7.00 (1)	VLA	-2.91 (1)	7.06 (1)	-9.97	-0.06	9.91
0847+612, Mrk 99	0.01282	9.21 (2)	NRT	-0.57 (2)	8.99 (1)	-9.57	0.22	9.78
Mrk 16	0.00777	8.94 (10)	GBT	-0.81 (2)	8.71 (1)	-9.52	0.23	9.75
J0859+3923	0.0019	7.10 (5)	GBT	-3.19 (1)	6.92 (1)	-10.04	0.25	10.29
CG 6	0.00656	8.42 (4)	Arecibo	-1.02 (4)	8.93 (1)	-9.95	-0.51	9.44
J0903+0548	0.0129	8.34 (5)	GBT	-1.42 (2)	8.05 (1)	-9.47	0.29	9.76
J0908+0517	0.00199	7.66 (5)	GBT	-3.25 (1)	5.86 (1)	-9.11	1.81	10.91
CG 10	0.00634	8.10 (4)	Arecibo	-1.92 (1)	7.54 (1)	-9.46	0.56	10.02
CG 13	0.00627	9.26 (4)	Arecibo	-1.21 (1)	7.68 (1)	-8.90	1.57	10.47
CG 14	0.00631	8.22 (4)	Arecibo	-1.23 (6)	8.43 (1)	-9.66	-0.21	9.44
Mrk 104	0.00738	8.73 (10)	GBT	-0.73 (2)	8.84 (1)	-9.57	-0.11	9.46
Mrk 1416	0.00779	8.71 (11)	Effelsberg	-1.07 (2)	7.54 (1)	-8.61	1.17	9.78
J0921+3944	0.01397	9.31 (5)	GBT	-1.29 (1)	7.89 (1)	-9.18	1.42	10.60
I Zw 18	0.00253	8.32 (7)	VLA	-1.26 (2)	6.90 (1)	-8.15	1.42	9.58
0937+2949	0.00168	7.40 (9)	NRT	-2.46 (1)	6.91 (1)	-9.37	0.49	9.86
AGC 198691	0.00172	6.82 (12)	Arecibo	-3.68 (1)	5.20 (1)	-8.88	1.63	10.51
0940+4025	0.01883	8.50 (9)	NRT	-0.96 (2)	7.38 (1)	-8.34	1.13	9.46
0940+544	0.00554	8.61 (2)	GBT	-1.85 (2)	7.59 (1)	-9.45	1.02	10.46
J0944+0936	0.00171	7.74 (5)	GBT	-2.35 (1)	7.95 (2)	-10.30	-0.21	10.09
SBS 0943+543	0.0053	7.07 (11)	Effelsberg	-1.58 (3)	6.89 (4)	-8.48	0.18	8.65
SBS 0943+563B	0.02	9.57 (11)	Effelsberg	-0.74 (2)	8.63 (1)	-9.37	0.94	10.31
Mrk 407	0.00529	9.16 (10)	GBT	-1.20 (2)	8.46 (1)	-9.66	0.71	10.36
Mrk 1426	0.00618	8.25 (11)	Effelsberg	-1.41 (6)	6.10 (4)	-7.51	2.15	9.65
CG 34	0.01730	8.43 (4)	Arecibo	-0.72 (2)	8.19 (1)	-8.91	0.24	9.15
Haro 22	0.00484	8.04 (4)	Arecibo	-1.75 (4)	7.86 (4)	-9.61	0.18	9.79
Mrk 714	0.00422	7.93 (4)	Arecibo	-1.66 (2)	8.24 (1)	-9.90	-0.31	9.59
Haro 23, UGCA 201	0.00457	8.06 (4)	Arecibo	-1.08 (2)	8.61 (4)	-9.69	-0.55	9.14
CG 55, KUG 1006+322	0.00485	8.22 (4)	Arecibo	-1.88 (2)	7.98 (1)	-9.85	0.24	10.09
Wa 5	0.00436	7.39 (4)	Arecibo	-1.81 (2)	7.41 (1)	-9.22	-0.02	9.20
Wa 6	0.01795	9.30 (4)	Arecibo	-0.67 (2)	8.75 (1)	-9.42	0.54	9.97
Mrk 27	0.00711	8.52 (10)	GBT	-1.61 (1)	8.19 (1)	-9.80	0.33	10.13
d1012+64	0.00062	6.02 (13)	GMRT	-3.43 (1)	6.93 (1)	-10.36	-0.91	9.45
Wa 8	0.0036	8.17 (4)	Arecibo	-1.39 (2)	8.10 (1)	-9.48	0.07	9.55
Mrk 32	0.00283	7.96 (10)	GBT	-2.11 (2)	7.44 (1)	-9.55	0.53	10.08
d1028+70	-0.00036	6.11 (13)	GMRT	-3.44 (1)	6.26 (1)	-9.70	-0.15	9.55
AGC 731457	0.00152	7.26 (1)	VLA	-2.49 (1)	7.15 (1)	-9.64	0.11	9.75
Wa 13	0.00181	9.00 (4)	Arecibo	-1.37 (2)	8.48 (1)	-9.85	0.53	10.37
1033+4757	0.0052	8.04 (9)	NRT	-2.03 (2)	7.08 (4)	-9.11	0.95	10.07
1033+531	0.00318	7.64 (14)	Effelsberg	-1.89 (2)	7.57 (1)	-9.47	0.07	9.53
VV794, Spider	0.00210	9.13 (10)	GBT	-1.05 (2)	8.98 (4)	-10.03	0.15	10.18
Mrk 1263	0.00442	8.65 (4)	Arecibo	-1.44 (2)	6.77 (4)	-8.21	1.89	10.10
CG 72	0.00512	8.49 (15)	NRT	-1.55 (2)	8.06 (1)	-9.60	0.43	10.04
Mrk 156	0.00463	8.64 (10)	GBT	-1.21 (2)	8.04 (1)	-9.26	0.60	9.86
Mrk 157	0.00464	9.07 (10)	GBT	-0.84 (2)	8.55 (1)	-9.39	0.52	9.91

Table A2 (cont'd)

J1055+5111	0.00457	7.58 (5)	GBT	-2.17 (1)	7.04 (1)	-9.21	0.55	9.75
Mrk 1271	0.00339	7.47 (4)	Arecibo	-1.18 (2)	8.28 (1)	-9.46	-0.80	8.65
CG 75	0.00425	7.84 (4)	Arecibo	-1.92 (2)	7.93 (1)	-9.85	-0.09	9.76
CG 76	0.00552	7.71 (4)	Arecibo	-1.91 (2)	7.97 (1)	-9.88	-0.26	9.62
SBS 1054+504	0.00459	7.51 (11)	Effelsberg	-1.75 (2)	8.20 (1)	-9.94	-0.69	9.25
1059+3934	0.01098	8.71 (9)	NRT	-1.42 (1)	7.90 (1)	-9.32	0.80	10.12
Haro 4	0.00216	7.55 (16)	VLA	-1.73 (2)	7.01 (1)	-8.73	0.55	9.28
SBS 1114+587	0.00561	7.86 (11)	Effelsberg	-1.61 (2)	7.97 (4)	-9.58	-0.11	9.47
J1119+0935	0.00331	7.97 (5)	GBT	-2.18 (1)	7.25 (1)	-9.43	0.72	10.15
SBS 1116+517	0.00446	8.05 (11)	Effelsberg	-1.71 (1)	7.23 (1)	-8.94	0.82	9.76
J1121+5720	0.00358	7.37 (5)	GBT	-2.81 (1)	7.05 (1)	-9.86	0.33	10.19
J1121+0324	0.00383	8.18 (5)	GBT	-2.43 (1)	6.69 (1)	-9.12	1.49	10.61
CG 103	0.00541	8.66 (4)	Arecibo	-1.05 (2)	8.49 (1)	-9.53	0.17	9.71
1123+644	0.00330	8.55 (2)	GBT	-1.52 (2)	8.29 (1)	-9.81	0.26	10.07
J1127+6536	0.00411	7.06 (5)	GBT	-2.83 (1)	7.11 (1)	-9.94	-0.05	9.89
J1128+5714	0.00556	7.94 (5)	GBT	-2.25 (1)	7.15 (1)	-9.40	0.80	10.20
Mrk 424	0.00647	8.62 (4)	Arecibo	-1.00 (6)	8.72 (1)	-9.72	-0.10	9.62
1128+573	0.00577	7.94 (14)	Effelsberg	-1.91 (2)	7.11 (1)	-9.01	0.83	9.85
Mrk 178	0.00078	7.11 (17)	GBT	-2.39 (1)	6.53 (1)	-8.92	0.59	9.51
Wa 23	0.00812	8.86 (4)	Arecibo	-1.00 (2)	8.68 (1)	-9.67	0.19	9.86
SBS 1137+589	0.00647	8.13 (11)	Effelsberg	-1.94 (6)	7.61 (1)	-9.55	0.52	10.07
Mrk 426	0.00518	8.84 (4)	Arecibo	-1.09 (2)	8.54 (1)	-9.63	0.29	9.93
Wa 25	0.00614	8.60 (4)	Arecibo	-1.43 (4)	7.28 (1)	-8.70	1.32	10.02
Wa 27	0.00608	8.84 (4)	Arecibo	-1.22 (2)	8.43 (1)	-9.64	0.41	10.06
Wa 28	0.00603	8.98 (4)	Arecibo	-1.41 (2)	7.78 (1)	-9.19	1.21	10.39
Mrk 747	0.00250	7.49 (4)	Arecibo	-1.78 (2)	7.86 (1)	-9.65	-0.37	9.28
CG 123	0.00616	8.37 (4)	Arecibo	-1.05 (2)	8.57 (1)	-9.62	-0.21	9.42
NGC 3870, Mrk 186	0.00241	8.17 (8)	GBT	-1.23 (2)	8.47 (1)	-9.70	-0.30	9.40
SBS 1144+591	0.00944	8.98 (11)	Effelsberg	-1.28 (1)	8.41 (1)	-9.70	0.56	10.26
1145+601	0.00420	8.06 (14)	Effelsberg	-1.49 (2)	8.18 (1)	-9.67	-0.12	9.55
J1148+5400	0.00866	8.45 (5)	GBT	-1.50 (3)	7.70 (1)	-9.20	0.75	9.95
Wa 34	0.0112	7.88 (4)	Arecibo	-1.22 (2)	8.25 (1)	-9.46	-0.37	9.10
Mrk 1460	0.00265	6.80 (11)	Effelsberg	-2.41 (2)	7.20 (1)	-9.61	-0.39	9.22
Mrk 641	0.00736	8.07 (4)	Arecibo	-1.20 (2)	8.37 (1)	-9.57	-0.30	9.27
CG 130	0.01091	8.57 (4)	Arecibo	-1.40 (2)	8.75 (1)	-10.15	-0.18	9.97
CG 142	0.00206	7.70 (4)	Arecibo	-2.09 (2)	8.01 (1)	-10.10	-0.31	9.78
Mrk 756	0.00495	8.79 (4)	Arecibo	-1.06 (2)	8.19 (1)	-9.25	0.59	9.84
CG 150	0.00204	7.50 (4)	Arecibo	-2.01 (2)	7.84 (1)	-9.84	-0.34	9.51
1203+592	0.01092	9.33 (2)	NRT	-0.64 (2)	8.93 (1)	-9.57	0.40	9.97
SBS 1205+557	0.0059	7.52 (11)	Effelsberg	-1.64 (2)	7.63 (1)	-9.27	-0.11	9.16
CG 159	0.02195	8.54 (4)	Arecibo	-0.95 (2)	8.31 (1)	-9.26	0.23	9.49
1208+531	0.00303	7.72 (14)	Effelsberg	-2.42 (2)	7.11 (1)	-9.53	0.60	10.13
NGC 4163	0.00055	7.18 (7)	VLA	-2.65 (1)	7.49 (1)	-10.14	-0.31	9.83
UM 483	0.0078	8.65 (4)	Arecibo	-1.19 (2)	8.12 (1)	-9.30	0.54	9.84
SBS 1211+540	0.00304	7.30 (11)	Effelsberg	-2.37 (2)	6.54 (1)	-8.91	0.76	9.67
1212+505	0.0134	8.48 (14)	Effelsberg	-1.37 (2)	7.97 (1)	-9.34	0.51	9.85
J1214+0940	0.00566	7.22 (5)	GBT	-2.37 (1)	7.67 (1)	-10.04	-0.46	9.58
CG 165	0.02837	9.00 (4)	Arecibo	-0.69 (2)	7.31 (1)	-8.01	1.69	9.69
J1215+5223	0.00051	7.24 (5)	GBT	-3.11 (1)	6.62 (1)	-9.72	0.63	10.35
Haro 28, NGC 4218	0.00241	8.15 (10)	GBT	-1.41 (2)	8.50 (1)	-9.91	-0.35	9.56
1213+597	0.01468	8.96 (2)	NRT	-0.34 (2)	9.39 (1)	-9.73	-0.43	9.30
VV 432	-0.00056	8.60 (10)	Arecibo	-1.69 (1)	8.08 (1)	-9.77	0.52	10.30
UM 491	0.00669	8.26 (4)	Arecibo	-1.13 (2)	8.10 (1)	-9.23	0.16	9.39
Wa 52	0.00861	9.09 (4)	Arecibo	-1.10 (2)	8.22 (1)	-9.32	0.87	10.19
Mrk 1323	0.00627	8.28 (4)	Arecibo	-1.34 (2)	8.56 (1)	-9.90	-0.28	9.62
AGC 749237	0.00124	7.76 (1)	VLA	-2.34 (7)	6.69 (1)	-9.03	1.07	10.10
NGC 4449	0.00068	9.48 (7)	VLA	-0.50 (2)	8.70 (1)	-9.19	0.78	9.98
1227+563	0.015	8.70 (14)	Effelsberg	-1.58 (1)	8.13 (1)	-9.71	0.57	10.28
CG 187	0.01435	9.21 (4)	Arecibo	-1.22 (1)	8.73 (1)	-9.94	0.49	10.43
CG 189	0.03105	9.38 (4)	Arecibo	-0.57 (2)	8.23 (1)	-8.80	1.15	9.95
UM 513	0.01248	8.54 (4)	Arecibo	-1.46 (1)	8.70 (1)	-10.15	-0.16	9.99
1241+549	0.01581	9.28 (2)	NRT	-1.32 (4)	8.37 (1)	-9.69	0.91	10.60
Haro 33	0.00316	8.53 (4)	Arecibo	-1.46 (2)	8.10 (1)	-9.56	0.43	9.99
Haro 9	0.00358	8.93 (10)	Arecibo	-0.47 (2)	8.81 (1)	-9.29	0.12	9.41
Mrk 224	0.003	7.35 (15)	NRT	-1.74 (2)	7.56 (1)	-9.30	-0.21	9.09
1248+518	0.0112	8.65 (14)	Effelsberg	-0.99 (2)	8.49 (1)	-9.48	0.16	9.64
Mrk 1338	0.00362	7.73 (4)	Arecibo	-2.26 (1)	8.29 (1)	-10.55	-0.56	9.99
VV 558	0.00071	6.85 (10)	GBT	-3.24 (1)	6.66 (1)	-9.90	0.19	10.09
UM 538	0.00313	6.88 (4)	Arecibo	-2.48 (2)	6.99 (1)	-9.47	-0.10	9.36
1318+520	0.01582	9.30 (2)	NRT	-0.47 (2)	9.21 (1)	-9.69	0.09	9.78
1323+483	0.01643	8.46 (2)	NRT	-0.84 (2)	8.06 (1)	-8.90	0.40	9.30
J1328+6341	0.00604	7.49 (2)	GBT	-2.52 (1)	7.28 (1)	-9.80	0.21	10.01
CPG 384	0.00080	7.46 (10)	GBT	-2.30 (2)	7.07 (1)	-9.37	0.38	9.75
Haro 38	0.00286	8.01 (4)	Arecibo	-1.83 (2)	7.88 (1)	-9.71	0.13	9.85
J1335+4910	0.00211	7.51 (5)	GBT	-2.86 (4)	6.86 (1)	-9.71	0.66	10.37
1341+594	0.01025	8.49 (2)	NRT	-1.33 (2)	7.72 (4)	-9.06	0.77	9.83

Table A2 (cont'd)

Mrk 277	0.00575	9.07 (10)	GBT	-1.70 (4)	7.61 (1)	-9.31	1.46	10.77
UM 618	0.01502	8.34 (4)	Arecibo	-1.17 (2)	8.08 (1)	-9.25	0.26	9.51
Wa 81	0.00650	7.94 (4)	Arecibo	-1.71 (2)	7.64 (1)	-9.35	0.30	9.65
1358+554E	0.01382	9.08 (2)	NRT	-0.76 (1)	8.09 (1)	-8.85	0.99	9.84
1359+504	0.00590	7.94 (14)	Effelsberg	-1.53 (2)	8.27 (1)	-9.80	-0.33	9.47
SBS 1400+461	0.00704	8.57 (11)	Effelsberg	-0.92 (2)	8.88 (1)	-9.80	-0.31	9.49
SBS 1401+490	0.00240	7.24 (11)	Effelsberg	-2.78 (1)	7.00 (1)	-9.78	0.24	10.02
J1404+5114	0.0059	8.18 (5)	GBT	-1.91 (3)	7.39 (1)	-9.30	0.79	10.09
1413+495	0.01284	8.94 (2)	NRT	-1.28 (2)	8.20 (4)	-9.48	0.74	10.22
1422+573	0.01057	9.17 (2)	GBT	-0.74 (6)	8.99 (1)	-9.74	0.17	9.91
1430+596	0.00604	8.40 (2)	NRT	-1.57 (2)	8.24 (1)	-9.81	0.16	9.98
SBS 1430+526	0.0109	9.09 (11)	Effelsberg	-0.74 (6)	8.76 (1)	-9.50	0.32	9.83
Mrk 1384	0.00762	9.02 (4)	Arecibo	-1.66 (2)	7.81 (1)	-9.47	1.21	10.68
Haro 43	0.00637	8.94 (4)	Arecibo	-1.24 (2)	7.19 (1)	-8.43	1.76	10.18
1435+516	0.00783	8.68 (14)	Effelsberg	-1.42 (1)	8.62 (1)	-10.14	0.05	10.10
Mrk 475	0.00186	6.56 (18)	GMRT	-2.40 (2)	6.71 (1)	-9.10	-0.14	8.96
Mrk 826	0.00239	7.32 (11)	Effelsberg	-2.21 (2)	7.65 (1)	-9.87	-0.33	9.53
II Zw 71	0.00418	8.87 (4)	Arecibo	-1.30 (2)	8.65 (1)	-9.95	0.22	10.17
SBS 1453+526	0.01088	8.57 (11)	Effelsberg	-1.05 (2)	8.34 (1)	-9.39	0.23	9.62
1455+443	0.01182	9.08 (2)	GBT	-0.75 (2)	8.79 (1)	-9.53	0.30	9.83
1506+553	0.01118	9.48 (2)	NRT	-0.59 (2)	9.39 (1)	-9.99	0.09	10.07
1509+527	0.01183	8.61 (2)	NRT	-0.83 (2)	8.94 (1)	-9.77	-0.33	9.44
1510+571	0.00215	7.17 (14)	Effelsberg	-2.89 (1)	7.07 (1)	-9.96	0.10	10.05
1519+496	0.01511	8.99 (2)	NRT	-0.61 (2)	9.08 (1)	-9.69	-0.09	9.60
Mrk 850	0.00734	8.17 (4)	Arecibo	-1.55 (4)	7.67 (1)	-9.22	0.50	9.72
1540+576A	0.0121	8.41 (14)	Effelsberg	-1.41 (2)	8.48 (1)	-9.89	-0.07	9.80
1551+601A	0.01040	8.70 (2)	NRT	-1.10 (2)	8.00 (1)	-9.10	0.70	9.80
1704+4332	0.00695	7.70 (9)	NRT	-1.80 (2)	6.78 (1)	-8.58	0.93	9.50
1707+565	0.01114	8.63 (2)	NRT	-0.77 (2)	8.72 (1)	-9.49	-0.09	9.40
1714+602	0.02013	9.27 (2)	NRT	-0.66 (2)	9.08 (1)	-9.74	0.19	9.93
J2053+0039	0.01328	9.09 (3)	Effelsberg	-2.26 (1)	7.53 (1)	-9.79	1.56	11.35
J2150+0033	0.01508	9.05 (3)	Effelsberg	-2.08 (1)	7.39 (1)	-9.47	1.65	11.13
2246+315	0.01285	9.23 (2)	NRT	-0.41 (2)	8.81 (1)	-9.22	0.42	9.64
NGC 7468	0.00695	9.42 (10)	Arecibo	-0.45 (4)	9.15 (1)	-9.61	0.27	9.87
Mrk 324	0.00538	8.42 (4)	Arecibo	-1.28 (1)	8.22 (1)	-9.50	0.20	9.70

Notes: Different columns are as follows: (1) Source name, (2) redshift, (3) logarithmic values of $M(\text{HI})$ in units of M_{\odot} , (4) telescope used, columns (5) to (9) are logarithmic values for star formation rate (SFR), stellar mass (M_{*}), specific star formation rate (sSFR), ratio of HI mass to stellar mass (f_{HI}) and depletion time scale τ_{HI} .

References for HI mass: (1) [Teich et al. \(2016\)](#), (2) [Thuan et al. \(1999\)](#), (3) [Filho et al. \(2013\)](#), (4) [Salzer et al. \(2002\)](#), (5) [Thuan et al. \(2016\)](#), (6) [Chengalur et al. \(2017\)](#), (7) [Lelli et al. \(2014b\)](#), (8) [Chengalur et al. \(2006\)](#), (9) [Pustilnik & Martin \(2007\)](#), (10) [Thuan & Martin \(1981\)](#), (11) [Huchtmeier et al. \(2005\)](#), (12) [Hirschauer et al. \(2016\)](#), (13) [Roychowdhury et al. \(2012\)](#), (14) [Huchtmeier et al. \(2007\)](#), (15) [Comte et al. \(1999\)](#), (16) [Bravo-Alfaro et al. \(2004\)](#), (17) [Ashley et al. \(2017\)](#), (18) [Jaiswal & Omar \(2020\)](#)

References for star formation rates: (1) Estimated using FUV luminosity without any correction, (2) Estimated using FUV luminosity corrected for dust extinction using W4 values, (3) MPA-JHU SDSS DR 7 catalog, (4) Using predicted FUV luminosity from SED fitting and corrected for dust extinction using W4 values, (5) [Teich et al. \(2016\)](#), (6) Estimated using NUV luminosity corrected for dust extinction using W4 values, (7) Estimated using NUV luminosity without any correction for dust extinction.

References for stellar mass: (1) This paper, (2) [Teich et al. \(2016\)](#), (3) [Lelli et al. \(2014b\)](#), (4) MPA-JHU SDSS DR 7 catalog.

All redshifts are from the SIMBAD database. In our analysis, for the sources in [Roychowdhury et al. \(2012\)](#), [Lelli et al. \(2014b\)](#), [Teich et al. \(2016\)](#) and [Ashley et al. \(2017\)](#), we use tip of the red giant branch (TRGB) distances used for estimating the HI mass in these papers. For VV 432, we use the Tully-Fisher distance from the extragalactic distance database ([Tully et al. 2009](#)). For VV 558, J1215+5223 and CPG 384, we use the TRGB distances from [McCall et al. \(2012\)](#), [Sabbini et al. \(2018\)](#) and [Tully et al. \(2013\)](#) respectively. For rest of the sources, HI masses from the literature are re-estimated according to cosmological luminosity distances. Abbreviations for different telescope names mean as follows: NRT: Nancay Radio Telescope, GBT: Green Bank Telescope, GMRT: Giant Metrewave Radio Telescope, VLA: Very Large Array